

The Bashgumbaz Complex (Tajikistan): Arc obduction in the Cimmerian orogeny of the Pamir

Stefano [Zanchetta](#)^{a,*}

stefano.zanchetta@unimib.it

James [Worthington](#)^b

Lucia [Angiolin](#)^c

Ernst Ja. [Leven](#)^d

Igor M. [Villa](#)^a

Andrea [Zanchi](#)^a

^aDipartimento di Scienze dell'Ambiente e della Terra, Università degli Studi di Milano Bicocca, Piazza della Scienza 4, 20126 Milano, Italy

^bDepartment of Geosciences, University of Arizona, 1040 E 4th street Tucson, AZ 85721, USA

^cDipartimento di Scienze della Terra, Università degli Studi di Milano, Via Mangiagalli 34, 20133 Milano, Italy

^dGeological Institute, Russian Academy of Sciences, Pyzhevski 7, Moscow, Russia

*Corresponding author.

Handling Editor: T. Tsunogae

Abstract

We present a new interpretation of the Bashgumbaz Complex (BSC), a fragment of a large mafic-ultramafic nappe exposed along the Alichur Valley in the Pamir, whose significance is of paramount importance for the understanding of the Cimmerian orogeny in South Pamir. The BSC is exposed along the contact between the SE and SW Pamir and consists of a low-grade metamorphic association dominated by gabbros and serpentinized harzburgites with minor bodies of quartzdiorite and plagiogranite tectonically coupled to basaltic and rhyolitic volcanic products. Tectonic slices of metasedimentary rocks are interleaved within the complex. The BSC, **with its upper part**, is in contact with a sedimentary unit rich in olistostromes with exotic blocks containing **a** Lower Permian fauna showing affinity with Central Pamir. The BSC is intruded by a Lower Cretaceous granitic body with a U-Pb zircon age of 117 Ma, crosscutting the whole complex. Petrographic, mineralogical and geochemical data suggest a supra-subduction-zone affinity for the gabbros and diorites. Significant enrichment in LILE and LREE compared to HREE, coupled with negative anomalies of Nb, Ti, Zr and other HFSE support this interpretation. U-Th-Pb dating of zircon from a diorite provides a lower Norian (ca. 222 Ma) youngest-crystallization-age constraint, suggesting that the BSC formed in a supra-subduction setting on the South Pamir terrane prior to the collision between Central and South Pamir blocks, **and** it was later underthrust and then obducted onto the southern margin of the closing Rushan-Pshart Ocean, which separated these two Gondwanan terranes during the Permian-Triassic. The obduction of the Bashgumbaz ophiolites can be considered as a time constraint for the collision between the South and Central Pamir terranes, which occurred within the framework of the Cimmerian orogeny that shaped the southern margin of Eurasia.

Keywords: Pamir; Cimmerian orogeny; **m**Magmatic arc; **t**Tectonic accretion

1.1 Introduction

Ophiolites found along suture zones within both collisional and accretionary-type orogens (e.g. [Dilek and Furnes, 2014](#)) represent a first-order proxy for the reconnaissance of plate boundaries among different terranes that have been amalgamated during continent-continent collisional processes. The geodynamic significance of ophiolites directly relates to their origin (e.g. mid-ocean ridge, continental margin, subduction-related, volcanic-arc type), time of emplacement and age. In collisional belts strongly affected by deformation and metamorphism, like the Pamir, complete ophiolites are rare. Relicts of dismembered ophiolitic complexes are commonly found, but their interpretation

in terms of geological significance is not always straightforward due to their often-poor preservation. Other markers that can help to reconstruct the large-scale orogen architecture are magmatic arcs (e.g. Şengör et al., 1993), which have played a key role in the understanding of the geodynamic setting of the Himalayas and Kohistan-Ladakh region (e.g. Bard, 1983; Coward et al., 1987).

This specifically holds true in those geodynamic frameworks that are characterized by processes of tectonic accretion, where multiple collisions of small micro-continents and/or island arcs progressively shift the position of arc activity with respect to the active subduction trench (Şengör et al., 1993). In these cases, magmatic arcs can provide hints on suture position between adjoining crustal blocks even if remnants of ophiolitic or subduction accretionary complexes are not preserved.

The Pamir belt, located NW of the Himalaya, affords one of the clearest examples of the progressive continental accretion occurring along the southern Eurasian margin across the entire Phanerozoic. They formed in response to the Cenozoic collision and indentation of India with Eurasia resulting in strong deformation and bending of pre-existing Palaeozoic to Mesozoic orogens (e.g. Burtman and Molnar, 1993; Schwab et al., 2004). Several crustal blocks connected along complex and poorly studied suture zones form the present-day tectonic architecture of this region. The extreme crustal shortening experienced by the Pamir during the indentation of India hinders straightforward correlations between tectonic terranes of the Himalaya-Tibet region with their potential continuations through the Pamir into Afghanistan and Iran.

Available palaeogeographic reconstructions suggest that the North Pamir was part of the southern Eurasian margin since the end of the Palaeozoic (e.g. Angiolini et al., 2016). Its southern portion, the Karakul-Mazar block, represents an island arc that developed above the Palaeotethys subduction zone during the Permian and Triassic (Schwab et al., 2004). To the south, Central and South Pamir, together with the Karakoram and part of the Qiangtang terrane, separated from Gondwana in the Early Permian due to the opening of the Neotethys. After drifting northward, they diachronously collided during the Mesozoic with North Pamir following the closure of the Palaeotethys Ocean (Angiolini et al., 2013a, 2013b; Robinson, 2015).

The Central and South Pamir are now joined along the Rushan-Pshart Suture (RPS), which extends E-W from the E-Pamir Fault to the valley of the Panji River (Figs. 1, 2; Burtman and Molnar, 1993, Burtman, 2010). This poorly understood suture zone was alternatively correlated with the Bangong-Nujiang Suture and even with the much younger Wasser-Panjao Suture of Afghanistan (Stampfli and Pilleveit, 1993; Schwab et al., 2004), or tentatively with the Longu Co-Shuanghu Suture (Angiolini et al., 2013a), which has been interpreted to separate the North and South Qiangtang terranes (Liu et al., 2011; Liang et al., 2012; Zhao et al., 2015). The RPS was strongly deformed and reworked during the intensive Cenozoic shortening of this region (Schwab et al., 2004; Stübner et al., 2013a) following the collision of the Indian subcontinent with Eurasia and its subsequent indentation. The thrust zone still contains a few isolated tectonic slices of serpentinite, which are interpreted as remnants of the Rushan-Pshart Ocean, which itself separated the South Pamir from Central Pamir. Due to the strong Cenozoic collisional overprint, the time of closure of the suture is still debated. Robinson (2015) and Angiolini et al. (2013a, 2015) favour a closure between the Late Triassic and Jurassic, whereas Leven (1995) and Schwab et al. (2004) suggested a Late Jurassic-Cretaceous event. Schwab et al. (2004) relate the suture zone to north-dipping subduction due to the occurrence of ophiolitic fragments in the South Pamir, the Bashgumbaz Complex, deriving from the obduction of Central Pamir onto South Pamir. Alternatively, Robinson et al. (2012) and Robinson (2015) suggest that the suture resulted from the south-dipping subduction of the Rushan-Pshart Ocean, given the position of Mesozoic intrusive rocks along the northern part of the South-East Pamir, without excluding a possible double subduction directed to both the north and south. Based on the analysis of the SE Pamir coeval sedimentary successions, Angiolini et al. (2013a) relate the remarkable unconformity occurring between the Permian-Triassic deformed sequence and the earliest Jurassic red sandstones exposed in the SE Pamir to the closure of the Rushan-Pshart Ocean, which culminated in the collision of the Central and South Pamir blocks.

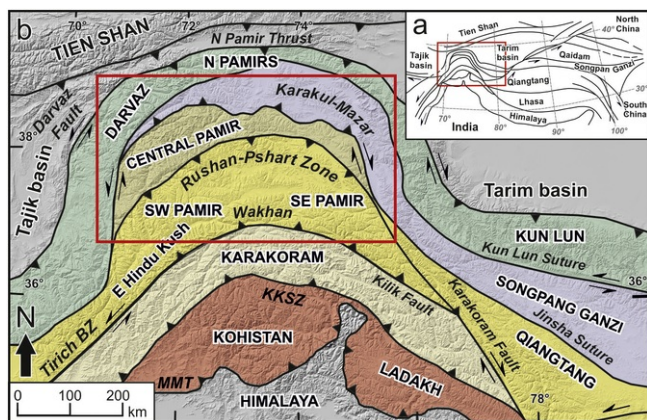


Figure 1. Fig. 1 (a) Tectonic scheme of Central Asia and Tibet area depicting the main sutures and at the regional scale. The area of figure 1(b) is highlighted in red. (b) Simplified scheme of the Pamir area with the main terranes represented in different

colours. Yellow shaded blocks (Central Pamir, South Pamir and Karakoram) are those derived from the Gondwana margin. The Pamir belts have been strongly deformed and forced to move northward in response to the Cenozoic indentation of India. The red rectangle in figure (b) indicates the areal extent of [Figure 2](#). MMT: Main Mantle Thrust; KKSZ: Karakoram-Kohistan Suture Zone. [\(For interpretation of the references to colour in this figure legend, the reader is referred to the web version of this article.\)](#)

Modified after [Angiolini et al. \(2013a, 2013b\)](#) with data from [Schwab et al. \(2004\)](#), [Zanchi and Gaetani \(2011\)](#), [Robinson et al. \(2012\)](#), [Zhao et al. \(2015\)](#).

alt-text: Fig. 1

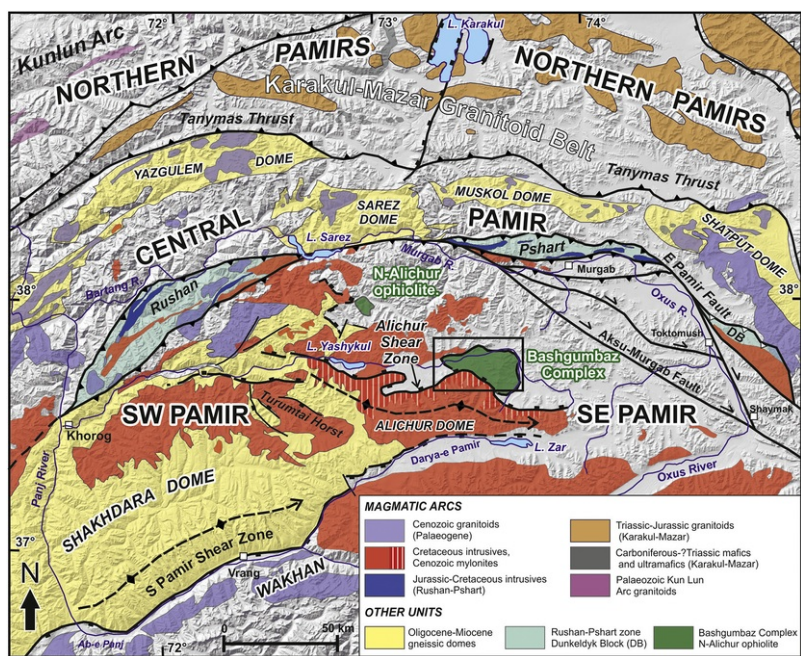


Figure 2. Tectonic setting of the Pamir with the main geological features. Intrusive and volcanic rocks are depicted in different colours reflecting their age. Triassic-Jurassic granitoids of the Karakul-Mazar arc are confined in the N Pamir block.

Cretaceous intrusives occur mainly in the South Pamir, whereas Cenozoic granites intrude both Central and S Pamir blocks. Jurassic to Cenozoic magmatic rocks occur in the Rushan-Pshart Zone and the Dunkeldyk block, at the boundary between Central and South Pamir. Widespread anatectic granites of Oligocene and Miocene age occur within the gneissic domes (yellow in the map). [\(For interpretation of the references to colour in this figure legend, the reader is referred to the web version of this article.\)](#)

Modified after [Angiolini et al. \(2015\)](#) and largely based on [Vlasov et al. \(1991\)](#), and [Schwab et al. \(2004\)](#).

alt-text: Fig. 2

The Bashgumbaz Complex (BSC) and the N Alichur ophiolites, which are altogether interpreted as fragments of a large, obducted ophiolitic nappe exposed along the Alichur Valley, represent a key element of the geology of the South Pamir ([Figs. 2 and 3](#)). These poorly studied units were interpreted in the past ([Pashkov and Shvol'man, 1979](#); [Shvol'man, 1978, 1980](#)) as a fragment of oceanic crust, possibly rooted within the Rushan-Pshart Suture ([Burtman and Molnar, 1993](#)). For this reason, a detailed analysis of its features and evolution is of paramount importance for the reconstruction of the collisional history of the South and Central Pamir.

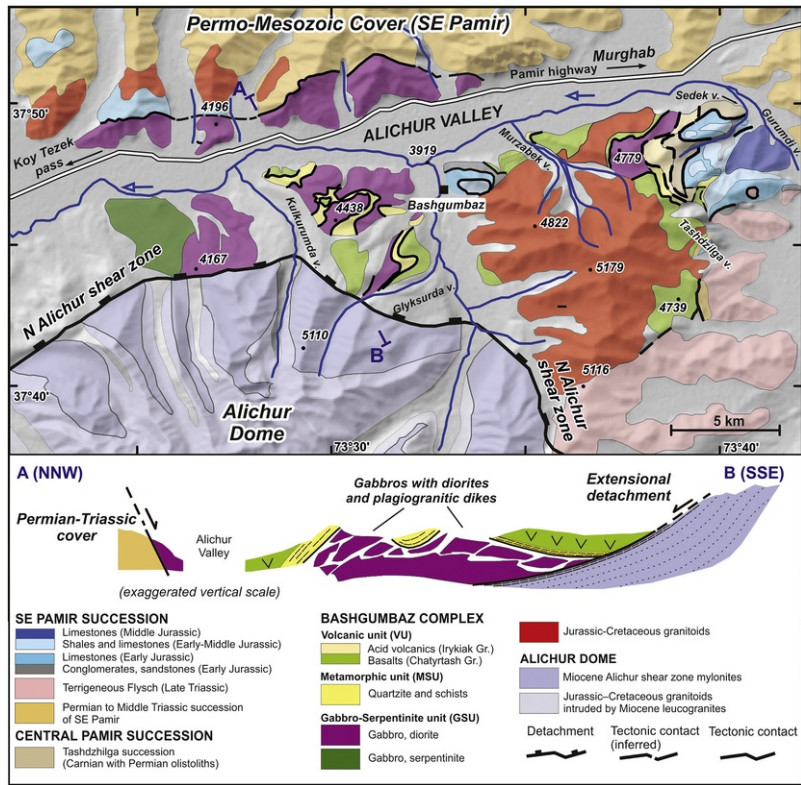


Figure 3. Fig. 3 Simplified geological map of the Bashgumbaz Complex (BSC), South Alichur Range, based on our own data and data from Shvolman (1980). Rocks attributed to the BSC crop out on both sides of the Alichur valley. On the north side a south-dipping normal fault marks the contact between the BSC gabbros and the Permian-Mesozoic cover of SE Pamir. The southern contact corresponds to the north-dipping Alichur Shear Zone, along which the Alichur Dome was exhumed in the Miocene (Stübner et al., 2013b). The schematic geological cross section represents the structural relationships occurring among the geological units exposed in the Bashgumbaz area.

alt-text: Fig. 3

Here, we present a new interpretation of the BSC, which will help to understand its significance in the frame of the Cimmerian collisions between South and Central Pamir. Petrologic, geochemical and radiometric analyses allow us to define the main features of this unit, which in our model represents a partially obducted magmatic arc that developed along the Rushan-Pshart suture zone.

2.2 Geological setting

The present-day setting of South Pamir (Figs. 1, 2) is dominated by the occurrence of a crustal-scale extensional detachment system that juxtaposes Permian to Cenozoic sedimentary succession of the SE Pamir against the gigantic basement domes of the SW Pamir (Schwab et al., 2004; Schmidt et al., 2011; Stübner et al., 2013a). The Shakh dara dome, which is the largest of these structures, exposes Precambrian metamorphic rocks with an Oligocene-Miocene high-grade overprint in its footwall (Schmidt et al., 2011). The Alichur dome, which extends E-W south of the Alichur Valley, consists of Jurassic to Cretaceous granitoids intruded by Miocene leucogranites in its footwall with a low-grade overprint. The footwalls of these domes were tectonically exhumed along low-angle, normal-sense, mylonitic shear zones, with up to 90 km of horizontal extension estimated for the Shakh dara dome (Fig. 2) that was balanced by crustal thickening in the Pamir fold-and-thrust belts and in the Tajik basin along the North Pamir foreland (Stübner et al., 2013b).

The SE Pamir forms the upper plate of the extensional system. This block is now bounded to the north by the Rushan-Pshart Zone; the eastern prolongation of the South Pamir Shear Zone (Fig. 1) separates it from Wakhan to the south. During the Permian, the SE Pamir was separated to the south from the Karakoram by the Wakhan basin (Angiolini et al., 2013a; Zanchi and Gaetani, 1994, 2011), and to the north from Central Pamir by the Rushan-Pshart Zone (Leven, 1995). The Lower Permian lava flows of SE Pamir (Angiolini et al., 2015) correlate with the basaltic lavas of the Pshart Zone, related to the opening of the Rushan-Pshart Ocean between the South and Central Pamir

(Novikov, 1979; Leven, 1995; Angiolini et al., 2015). Averaged palaeomagnetic data obtained from Upper Permian units (Davydov et al., 1982) suggest that the SE Pamir was situated $8.5 \pm 7^\circ$ north of the equator by the Permian-Triassic boundary (Angiolini et al., 2015).

The SE Pamir block consists of a Permian–Triassic succession characterized by a thick Upper Carboniferous to Lower Permian terrigenous unit at the base, overlain by Permian cherty limestones with lava flows and Triassic shallow limestones, which record the evolution of a faulted passive margin that evolved during the rifting and drifting of the block from Gondwana (Angiolini et al., 2015 and references therein). An important unconformity separates strongly deformed Permian-Triassic units from the basal Jurassic deposits, which comprise sandstones and conglomerates (Darbasatash Group) conformably covered by Hettangian shallow-sea limestones (Dronov et al., 2006). According to Angiolini et al. (2013a), the unconformity records the closing of the Rushan-Pshart Suture, which registers the collision between South and Central Pamir terranes. Discontinuous marine ~~terrigenous~~-~~terrigenous~~ and carbonate deposits represent the youngest sedimentary record, extending to the late Cenozoic (Vlasov et al., 1991; Dronov et al., 2006). Jurassic and Cretaceous granitoids, which are related to the northward subduction of the Neotethys active south of the Karakoram, pervasively intruded the SW and SE Pamir, and the Hindu Kush blocks (Faisal et al., 2016 (Add a reference: Chapman et al., 2018.)). Palaeogene and Miocene continental deposits are also exposed in the area, although ages are not yet precisely constrained (Vlasov et al., 1991). Post-Triassic tectonic structures in the SE Pamir consist of a N-verging thrust stack (Ruzhenstev & Shvol'man, 1982), which is mainly related to Cenozoic crustal shortening (Stübner et al., 2013a).

3.3 Field aspects and structural setting of the Bashgumbaz Complex and surrounding units

The Bashgumbaz Complex (BSC) is exposed along the boundary between the SW and SE Pamir in the Alichur valley and spans ca. 10 km N-S and ca. 25 km E-W (Fig. 3). It consists of a low-grade metamorphic association of serpentinized harzburgites and gabbros with minor bodies of diorites and plagiogranites, greenschist-facies metasedimentary rocks and basaltic to rhyolitic volcanic successions (Shvol'man, 1978, 1980). A ~~peculiar~~-terrigenous unit including carbonate olistostromes with exotic Permian and Triassic faunas (Dronov and Leven, 1990) is tectonically interleaved in the upper structural level of the BSC. Small isolated occurrences of a similar unit with volcanic rocks crop out along the northern side of the Alichur Valley in a similar tectonic position close to the boundary between SW and SE Pamir (Fig. 2). To the SW, the BSC is in tectonic contact ~~along a regional detachment~~ with gneisses and mylonitic Cretaceous granites of the Alichur Dome, which is part of SW Pamir, ~~along a regional detachment~~ (Schwab et al., 2004; Schmidt et al., 2011; Stübner et al., 2013a, 2013b). To the N, the BSC represents the hangingwall block of a ~~moderately~~-S-dipping normal fault (Stübner et al., 2013a) that brings in contact the BSC with the Permian-Mesozoic cover of SE Pamir. Along the eastern margin of the complex, low- to medium-angle shear zones represent the contact between the BSC including the structurally overlying Upper Triassic turbidites (Fig. 3) and a Jurassic succession consisting of limestones with minor conglomerates and sandstones at its base.

3.1.3.1 The Bashgumbaz Complex

The BSC comprises three units. (1) The Gabbro-Serpentinite unit (GSU) is the primary unit and chiefly consists of gabbros, metabasites of various types and serpentinites. This unit forms about the 70% of the areal extent of the complex and it widely crops out along the Kulkurumda and Glyksurda valleys, to the east and north of the Bashgumbaz village, respectively (Fig. 3). Gabbros and diorites also crop out on the northern flank of the Alichur valley (Fig. 3), where they are in tectonic contact with Jurassic sedimentary rocks or the Permian-Mesozoic cover of the SE Pamir. (2) The Metamorphic unit (MSU), consisting of phyllites and mica schists that are tectonically interleaved with gabbros of the GSU, and occurs along the watershed between the Kulkurumda and Glyksurda valleys. (3) The Volcanic Unit (VU), ~~consisting consists~~ of basalts (Chatyrtash Group of Shvol'man, 1978, 1980) and acidic volcanics (Irykiak Group of Shvol'man, 1978, 1980) with a poorly defined age (Triassic?). Where observed, the contact between this unit and the GSU is always marked by mylonitic shear zones (Fig. 4c). The southern limit of the Bashgumbaz Complex is defined by the top-to-north Alichur Shear Zone (Stübner et al., 2013a), which bounds the Cenozoic Alichur dome to the north (Schwab et al., 2004; Stübner et al., 2013a). South and east of the Bashgumbaz village, the BSC is intruded by a two-mica granite pluton with ca. 10 ~~x~~ ~~x~~ 15 km exposure (Figs. 3, 5b). Minor undeformed acidic dikes, likely related to the main intrusive bodies, intruded the complex east of Bashgumbaz (Fig. 4e).

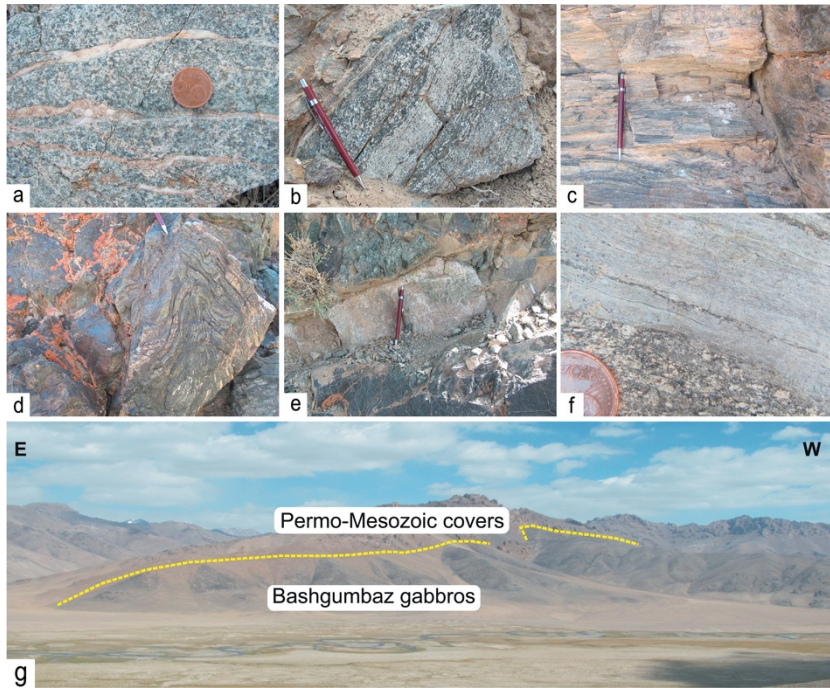


Figure 4. Field aspect of the main lithologies of the BSC. (a) Medium- to fine-grained isotropic gabbros of the GSU. The occurrence of carbonate-bearing veins is fairly common close to the contacts with the other subunits. (b) Flaser to protomylonitic texture developed in a gabbro of the GSU. (c) Mylonites within the Chatyrtash basalts at the contact with gabbros of the GSU, Glyksurda valley (Fig. 3). (d) Folded mylonites of the Chatyrtash basalts; fold axes broadly trend N-S, with steep axial planes: these trends are coherent with the Cimmerian regional deformation described in Angiolini et al. (2013a, 2013b). (e) A granitic dike, belonging to the Cretaceous Bashgumbaz granite, intruding gabbros of the GSU west of the Bashgumbaz village. (f) Gneiss-derived ultramylonites along the North Alichur Shear Zone (Fig. 3). (g)

Panoramic view of the contact between the BSC and the Permian-Mesozoic cover of the SE Pamir on the northern side of the Alichur valley.

alt-text: Fig. 4

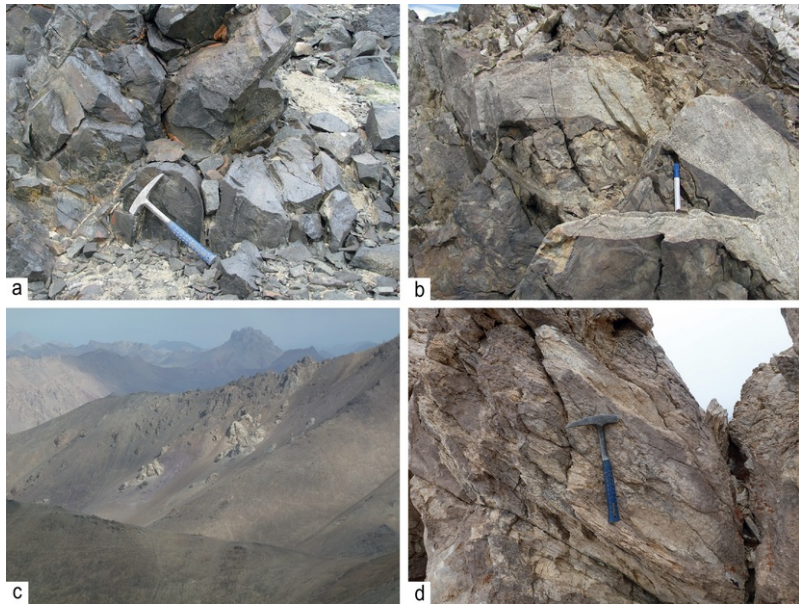


Figure 5. (a) Pillow structures in the Chatyrtash basalts (Murzabek valley, Fig. 3). (b) The Cretaceous Bashgumbaz granite intruding lavas of the Chatyrtash group along the Murzabek-Sedek valley drainage divide. (c) Carbonate olistoliths in the Tashdzhilga flysch, view towards E along the Sedek valley (Fig. 3). (d) Massive olistolith limestones intersected by a disjunctive cleavage.

alt-text: Fig. 5

3.1.1.3.1.1 The Gabbro-Serpentinite unit (GSU)

The ultramafic-gabbro unit comprises gabbros with minor diorites, quartz diorites and plagiogranites, as well as variably serpentinized harzburgites that crop out at the western margin of the complex. Isotropic gabbros (Fig. 4a) comprise most of the complex, with minor leucogranite and pegmatite lenses. Plagiogranites occur as ca. 1-30 m-wide lenses along the ridge on the left bank of the Glyksurda valley, as well as on the ridge between the Murzabek and Sedek valleys (Fig. 3). Both mafic and ultramafic rocks of the GSU are locally deformed to various degrees. Deformation is primarily localized along narrow shear zones in the southern part of the complex, whereas it becomes more widespread close to the tectonic contact with the Permian and Mesozoic sediments in the north, where gabbros are almost completely transformed into mylonitic amphibolites and mafic schists (the “gneiss-like” facies of Shvol'man, 1978, 1980). Gabbros with flaser to protomylonitic textures (Fig. 4b) also occur at the contact with the basalts of the Chatyrtash Group and the metasedimentary unit. Lens-shaped diorite and quartz-diorite bodies occur within gabbros. The primary intrusive relationships between the two rock types are erased by minor shear zones that developed at the expense of the finer grained diorites along the contacts with hosting gabbros. Gabbros are mostly isotropic and medium-grained (Fig. 4a), sometimes displaying a poorly defined layering with alternate plagioclase- and mafic-rich domains. A weak foliation is identified approaching shear zones, which turns into a flaser or protomylonitic texture within them (Fig. 4b), where diffuse carbonate veining is commonly observed (Fig. 4a). A low-grade (up to greenschist-facies) metamorphism affects the entire unit. Metamorphism always accompanies deformation, whereby magmatic fabric elements and minerals are better preserved in non-deformed samples, whereas metamorphic amphibole, plagioclase and chlorite grow along a non-penetrative foliation (see Section 4).

3.1.2.3.1.2 The Metamorphic Unit (MSU)

A metasedimentary unit composed of mica schist, quartzite, and minor calcschists is sandwiched between the GSU and the Volcanic Unit (VU) west of Bashgumbaz, between the Kulkurumda and Glyksurda valleys (Fig. 3). Thin slices of this unit also crop out on the north side of the Alichur valley, within the sheared gabbros of the GSU. Mica schist and calcschists are metamorphosed at greenschist-facies conditions, with white mica, chlorite and quartz that crystallize as new mineralogical phases in mica schist. Calcite and opaque minerals occur in calcschists, together with white mica and minor quartz. Small outcrops of quartzite and phyllite, occur on the E-W ridge between the Kulkurumda valley and Bashgumbaz. The metamorphic rocks are here strongly foliated or mylonitic, with very fine-grained chlorite and white mica whose shape preferred orientation marks the mylonitic foliation.

Mineralogical relicts, that likely suggest higher metamorphic conditions prior to mylonitization, have been found in only one sample (13P19; Table 1) of a mylonite derived from a garnet-bearing biotite gneiss, cropping out along the north side of the Alichur valley. Pre-kinematic garnet porphyroblasts almost completely substituted by chlorite aggregates are wrapped by the mylonitic chlorite + white mica foliation. Small (ca. 1.5–2 mm of maximum size) and strongly deformed relicts of biotite are

rarely preserved within strain shadows around garnet porphyroblasts.

Table 1. Sample description and location.

alt-text: Table 1

Sample	Tectonic unit	Rock type	Mineralogy																				Coordinates			
			Ol	Cpx	Opx	Pl	Amp	Ep	Chl	Cal	Rt	Ttn	Tc	Mt	Ox	Qtz	Bt	Wm	Grt	Fe-Ti ox	Sp	Ap	Zr	Tur	Latitude (N)	Longitude (E)
TZ-0	Bashgumbaz complex	Gabbro				x	x		x						x										37° 47' 04.10" N	73° 30' 43.30" E
TZ-3	Bashgumbaz complex	Olivine gabbro	x	x		x	x		x						x										37° 47' 04.10" N	73° 30' 43.30" E
TZ-4	Bashgumbaz complex	Gabbro				x	x		x						x										37° 47' 04.10" N	73° 30' 43.30" E
13P17	Bashgumbaz complex	Amphibolite																							37° 48' 24.73" N	73° 28' 58.58" E
13P20	Bashgumbaz complex	Diorite				x	x	x							x	x							x	x	37° 48' 36.25" N	73° 28' 49.73" E
13P23	Bashgumbaz complex	Olivine gabbro	x	x		x	x								x										37° 46' 48.57" N	73° 30' 59.51" E
13P24	Bashgumbaz complex	Olivine gabbro	(x)	x		x																x			37° 47' 10.93" N	73° 30' 59.51" E
13P25	Bashgumbaz complex	Gabbro		x		x									x										37° 47' 2.11" N	73° 31' 09.62" E
13P28	Bashgumbaz complex	Gabbro		x		x	x								x										37° 45' 35.31" N	73° 31' 09.61" E
13P31	Bashgumbaz complex	Quartz diorite		x		x	x				x				x	x								x	37° 44' 11.94" N	73° 30' 50.04" E
13P16	Metamorphic basement	Mylonitic schists																							37° 48' 20.23" N	73° 28' 58.80" E
13P19	Metamorphic basement	Biotite gneiss				x																			37° 48' 30.56" N	73° 28' 50.52" E
13P29	Metamorphic basement	Mafic mylonite					x	x	x	x					x	x									37° 44' 36.60" N	73° 31' 05.55" E
13P21	Alitichur granite	Two-mica granite				x			x						x	x	x	x		x			x	x	37° 46' 17.07" N	73° 34' 18.61" E

Notes: Mineral abbreviations. Amp: amphibole; Ap: apatite; Bt: biotite; Cc: calcite; Chl: chlorite; Cpx: clinopyroxene; Ep: epidote; Fe-Ti-ox: Fe-Ti oxides; Grt: garnet; Mt: magnetite; Ol: olivine; Pl: plagioclase; Pyr: pyrite; Qtz: quartz; Rt: rutile; Serp: serpentine; Stp: stilpnomelane; Tc: talc; Ttn: titanite; Wm: white mica; Zr: zircon.

3.1.3.3.1.3 The Volcanic Unit (VU)

Basaltic lava flows with locally well-preserved pillow structures occur structurally above the GSU and MSU (Fig. 3). These basalts, reported in Shvol'man (1978, 1980) as the Chatyrtash Group, are non-deformed and substantially non-metamorphosed, displaying only weak recrystallization up to anchimetamorphic conditions, mainly along the contact with the structurally underlying GSU. The contact between volcanic rocks and GSU or the MSU, where exposed, are invariably tectonic. In detail, we observed ca. 4–5 m-thick brittle-ductile shear zones developed at the contact between the Chatyrtash basalt and the underlying gabbros (GSU) or mica schists (MSU).

The Chatyrtash basalts occur as lava flows with a massive texture, intercalated with flows displaying well-preserved pillow structures (Fig. 5a). The individual lava flows are almost invariably often separated from one another by intervening 1–3 m-thick layers of hyaloclastitic breccia.

A series of intermediate to acidic volcanic rocks and minor volcanoclastic layers (Irikyak Group of Shvol'man, 1980) is exposed along the Murzabek-Sedek drainage divide (Fig. 3). The Irikyak unit consists of dacitic to rhyolitic, greenish to lilac-coloured lava flows that are intercalated with pyroclastic beds, containing volcanic breccias of foam lavas and minor volcanoclastic sediments. Shvol'man (1978, 1980) reported a loosely constrained Early Cretaceous K-Ar age (124 Ma) for this unit. Dronov et al. (2006) suggested instead a Late Triassic age based on the conformable contact with the underlying unit (no fossils have been until now reported from the Irikyak Group).

The Bashgumbaz Cretaceous granite intruded both the GSU and the VU. Intrusive contacts between granite and the Chatyrtash basalts are exposed along the ridge on the left bank of the Murzabek valley (Figs. 3 and 5b).

3.1.4.3.1.4 Structural features of the Bashgumbaz Complex

The Early Jurassic age for the Darbasatash Group, which unconformably overlies the Tashdzhilga unit and the Chatyrtash basalts immediately west of Bashgumbaz (Fig. 3), provides an Early Jurassic youngest-age constraint for the deformation, metamorphism, and obduction of the Bashgumbaz Complex.

The GSU (and the Bashgumbaz Complex, more broadly) is bounded to the southwest by the Miocene, top-to-the-north, mylonitic Alichur Shear Zone, which separates the Bashgumbaz Complex in the hangingwall from the Alichur dome in the footwall (Figs. 2 and 3; Stübner et al., 2013a). The Alichur Shear Zone is up to 1 km thick and primarily comprises mylonites, ultramylonites (Fig. 4f) and localised localized cataclasites, which record ductile and brittle deformation and consistently display top-to-the-N kinematic indicators. Our structural measurements confirm that the mylonitic foliation dips gently N-NE (Fig. 6f) with a down-dip stretching lineation.

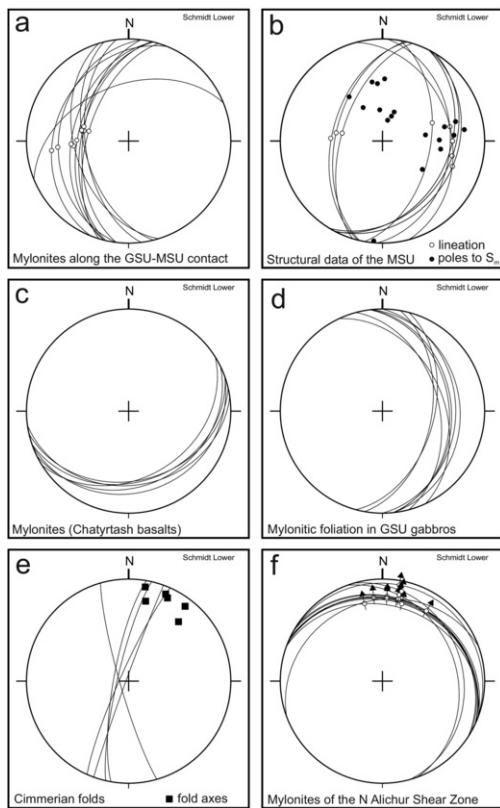


Figure 6. Fig. 6 Synthetic stereoplots of the main structural elements of the BSC. (a) W-dipping mylonites, mainly derived from pelitic schists, along the contact between the GSU and the MSU. (b) Stereographic projection of mylonitic (great circles) and non-mylonitic foliation within the MSU: both foliations dip alternatively to the WNW or ESE. (c) SSE-dipping mylonites along the basal contact of the Chatyrtash basalts with the underlying GSU; data from the Kulkurumda and Glyksurda valley areas (Fig. 3). (d) mylonitic and proto-mylonitic foliation in gabbros of the GSU. (e) fold axial planes and fold axes related to folds, of supposed Cimmerian age, within the MSU. (f) Mylonitic and ultra-mylonitic foliation along the North Alichur Shear Zone, SW of the Bashgumbaz village (Fig. 3).

alt-text: Fig. 6

The unconformity below the Darbasatash Group, the Alichur Shear Zone (Stübner et al., 2013a) and the normal fault on the northern flank of the Alichur valley (Fig. 3) thus represent the major contacts that delimit the Bashgumbaz Complex. The BSC is exposed in an asymmetric composite graben rather than in a tectonic window as suggested in the past (Shvol'man, 1978, 1980). The recognition of the BSC as a graben is of utmost importance as it reverses the structural relationships between the BSC and adjacent units, whereby we now interpret the BSC as the upper structural unit.

The deformation in the several units that are grouped in the Bashgumbaz Complex is localized along shear zones developed between units or along lithological contacts within a single unit. The contact between gabbros of the GSU and mica schist of the MSU on the eastern side of the Kulkurumda valley consists of several m-thick shear zone with mylonites derived from both gabbros and schists. The mylonitic foliation dips 30°–50° to the W (Fig. 6a). Down-dip lineations are ubiquitous but poorly developed kinematic indicators inhibited sense-of-slip determination in the field. The contact between GSU and MSU displays similar features, as one observed on the ridge to the N of the Glyksurda River (Fig. 3), where mylonites dip to the E. Shear zones are widespread also within each unit. Protomylonitic to flaser gabbros occur ca. 3.5 km WNW of Bashgumbaz village (Figs. 3 and 4b); foliation dips E- to SE-wards with dip angles between 25° and 35° (Fig. 6d). Shear zones within the MSU dip alternately to the WNW or ESE, with a down-dip lineation defined by stretched quartz or white mica (Fig. 6b). A similar pattern emerges also for the main foliation in mica schists and calcschists: foliation planes dip NW to ESE (Fig. 6b).

Variability of the attitude of foliation and mylonitic shear zones in the GSU is accounted for by a network of nearly upright folds with steeply WNW-dipping axial planes and gently NNW-plunging fold axes (Figs. 4d and 6e). Structures similar in style and orientation affect the pre-Jurassic succession of the SE Pamir north and east of the Alichur valley (Angiolini et al., 2013a). Here, the Lower Jurassic red beds of the Darbasatash Group unconformably overlie intensively folded and faulted Permian-Triassic strata. We interpret this deformation to record the collision between the SE Pamir and Central Pamir terranes within the framework of the Cimmerian orogeny (Angiolini et al., 2013a).

3.2.3.2 Units adjacent to the Bashgumbaz Complex

The volcanic and volcanoclastic rocks of the Irikyak Group (Shvol'man, 1978, 1980) are overthrust by the olistolith-bearing succession of the Tashdzhilga unit, which crops out along the Tashdzhilga and Sedek Valleys (Fig. 3). These olistoliths-bearing terrigenous flysch show close similarities with the Upper Triassic flysch of the SE Pamir (Dronov and Leven, 1990). The Jurassic succession of SE Pamir crops out on the northern flank of the Alichur valley, near the Bashgumbaz village, and along the Sedek and Gurumdi valleys (Fig. 3). The base of this succession consists of reddish conglomerates and sandstones of the Darbasatash Group that rest unconformably on the other described units (Angiolini et al., 2013a).

3.2.1.3.2.1 The Tashdzhilga unit

The Tashdzhilga Group chiefly consists of deformed siltstones with lens-shaped sandstones, as well as fine-grained conglomerates. Sandstones are often reddish and contain abundant volcanoclastic materials (Shvol'man, 1980). The peculiar feature of this unit is the occurrence in its upper part of several-tens-of-meters-sized olistoliths (Fig. 5c) embedded in a reddish to violet volcanoclastic matrix. Most of the olistoliths consist of whitish to grey coloured, massive to well-bedded limestones (Fig. 5d). Large blocks of acidic volcanic rocks (up to 10 m in size) and subordinate mafic clasts also occur. Dronov and Leven (1990, their Fig. 2) indicate close relationships between this unit and the Upper Triassic terrigenous flyschoid deposits exposed in the SE Pamir, especially the North Alichur successions (Dronov et al., 1989). Based on foraminifer assemblages, previous authors (Dronov, 1986; Dronov and Leven, 1990) attributed a Permian age to the olistoliths. They identified Asselian to lower Sakmarian, Bolorian to Kubergandian (Kungurian) and even Dzhulfian (Wuchiapingian) foraminifer assemblages within different blocks. The Asselian-Sakmarian fusulinid associations are dominated by species of *Sphaeroschwagerina* and show affinities with the Kalaktash fusulinid faunas present in Central Pamir and even in the Darvaz range, which is part of North Pamir (Dronov and Leven, 1990; Leven, 1993); however, *Sphaeroschwagerina* is extremely rare in Central Pamir. Noteworthy Asselian to Sakmarian fusulinids are completely absent in SE Pamir (Leven 1967; Grunt & Novikov, 1994; Angiolini et al., 2015), making their occurrence vs. absence a good palaeobiogeographical marker. The occurrence of Asselian-Lower Sakmarian fusulinids in some of the Tashdzhilga olistoliths thus suggests a stronger affinity with Central rather than with SE Pamir. Upper Lower Permian and Middle Permian fusulinids are instead widespread both in SE, Central and North Pamir, with upper Lower Permian fusulinids that are peculiar/typical of the West Pshart Zone (Leven, 1995). Shvol'man (1978, 1980) reported the occurrence of reworked Permian and Triassic corals, which differ from the typical faunas of SE Pamir. According to Pashkov and Shvol'man (1979), similar Triassic coral assemblages occur in the Ladinian to Carnian formations of the Rushan-Pshart Zone. Leven (1995) described the same coral association in the lower part of the Gumbekol Group and assigned it a Carnian age. Altogether, these data indicate that the Tashdzhilga olistoliths were not derived from SE Pamir, but possibly from Central Pamir or the Rushan-Pshart Zone.

3.2.2.3.2.2 The Jurassic succession

The deformed Permian-Triassic succession of SE Pamir is unconformably covered by red conglomerates and sandstones (the Darbasatash Group, Fig. 3), which are overlain by Hettangian shallow-sea limestones of the Gurumdi Group (Dronov et al., 2006). Near Bashgumbaz village, the base of the Jurassic comprises ca. 20-50 m-thick, red conglomeratic beds. The conglomerates contain clasts of greenish acidic to intermediate volcanic pebbles, as well as cm-sized clasts of SE Pamir Permian limestones. Monocrystalline volcanic quartz is abundant, as well as up to 1-1.5 cm clasts with a characteristic granophyric texture. Occasional weathered clasts of plagioclase cumulates and leucogranite occur as well. Collectively, these observations indicate the unroofing of the upper part of an acid volcanic arc (Angiolini et al., 2013a). Dronov et al. (2006) described a similar situation along the Sedek and Irikyak valleys, where the Dzhanbulak Group, which consists of 200 m of sandstones and conglomerates, overlies the Permian-Triassic strata along a transgressive contact. The Djanbalus terrigenous/terrigenous deposits could be considered analogous to the Darbasatash Group conglomerates and sandstones.

4.4 Petrography and mineral chemistry of rocks from the GSU

We studied the petrography of gabbros and diorites of the GSU in detail. Serpentinized harzburgites have been not investigated because they are strongly weathered and lack preserved relicts of the primary peridotite mineral assemblages. Pervasive, secondary carbonate and quartz veins in these samples also render them problematic because they hamper the reliability of bulk-rock analyses.

4.1.4.1 Methods

Thin sections of rocks of the analysed samples were/was/were polished and carbon coated. Textural and mineralogical features were inspected using back-scattered electron (BSE) and secondary electron maps and quantitatively characterized by electron microprobe analyses. Analyses were performed at the Earth Science Department of the University of Milano on a Jeol JXA 8200 Superprobe equipped with five wavelength-dispersive spectrometers (WDS). Analyses were conducted with an ~1 µm beam diameter at conditions of 15 kV and 5 nA of probe current. Natural silicates and oxides were used as standards. All standards were calibrated within 0.5% at one standard deviation. Raw data were corrected using a Phi-Rho-Z quantitative analysis program.

4.2.4.2 Results

The GSU gabbros are commonly isotropic, medium- to fine-grained, and display hypidiomorphic textures with rare pegmatoid lenses. Plagioclase is the most abundant phase in most gabbroic rocks (up to 55-60% by vol.), followed by amphibole and clinopyroxene. Olivine gabbros are restricted to the left bank of the Glyksurda Valley, just to the W of the Bashgumbaz village. Even in these samples (13P23, 13P24) olivine occurs in low modal amounts

(5–7% by vol.) and is usually included as anhedral crystals in clinopyroxene or plagioclase. Almost all the gabbro samples that we analysed contain partially retrogressed brown magmatic hornblende that defines the intercumulus phase between euhedral-subhedral plagioclase and clinopyroxene. Altogether, textures described for these samples indicate a crystallization sequence olivine-plagioclase-clinopyroxene-amphibole.

Plagioclase lacks zoning in most samples and has a uniform anorthite content of An_{55-60} (Table 3). The exceptions are samples TZ3, 13P24 and 13P28, which have Ca-rich cores (An_{65-73}) (Fig. 7c) and rims with decreasing Ca-concentration (An_{50-60}). Clinopyroxene is broadly diopsidic augite in composition (Fig. 7d), with $xMg(Fe_{tot})$ ranging from 0.72–0.83 (highest in samples 13P23 and 13P24, Table 3). Ti concentration is fairly low with TiO_2 of 0.25–0.95 wt%. Actinolitic amphibole (Amp_2) has grown on clinopyroxene rims in some samples. Brown amphibole cores (Amp_1), which are likely magmatic, are Mg-hornblende according to the Leake et al. (1997) classification scheme (Fig. 7a). Amphibole rims (Amp_2) display instead Al-poor compositions, shifting towards the actinolite and ferroactinolite end members (Fig. 7a). Within shear zones, Amp_1 is not preserved and undergoes diffuse recrystallization into tiny Amp_2 with a shape preferred orientation, which parallels a poorly developed compositional layering defined by amphibole- and plagioclase-rich layers. Olivine crystals included in plagioclase and clinopyroxene have a forsterite content of For_{85-90} (Table 3).

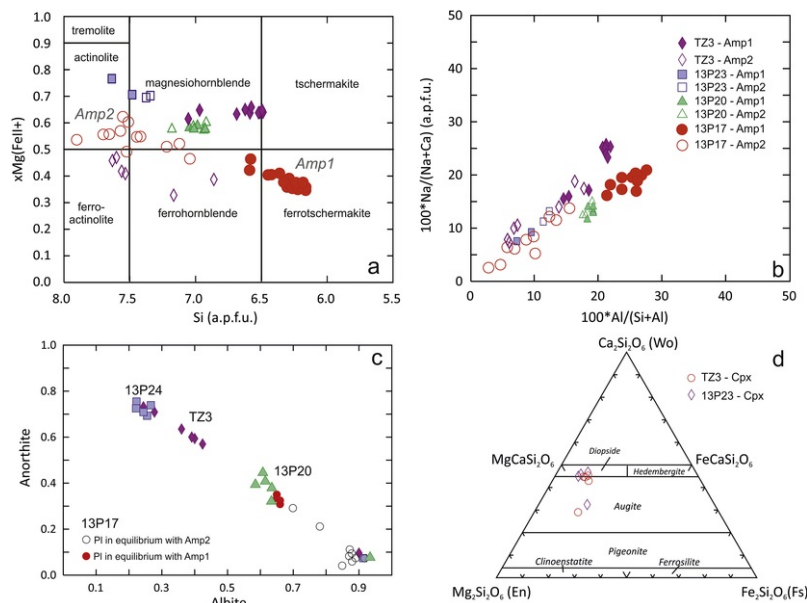


Figure 7. (a) Compositional classification of amphibole from the GSU following the classification scheme of Leake et al. (1997). Magmatic amphibole plot in magnesiohornblende compositional field. (b) Ca and Al contents of amphibole from the GSU and the MSU expressed relative to Na and Si, respectively. (c) Plagioclase from gabbros, diorites and amphibolites. Plagioclases from gabbros display higher Ca-content, with cores up to An_{75} . (d) Classification diagram of clinopyroxenes from rocks of the GSU.

alt-text: Fig. 7

Deformed gabbros from shear zones exhibit strong textural modification and mineralogical re-equilibration, which accompanied greenschist-facies metamorphism. This greenschist-facies overprint had the following effects: (1) magmatic amphibole (Amp_1) breakdown to actinolitic amphibole (Amp_2); (2) saussuritization of Ca-rich plagioclase; (3) formation of albitic rims on An-rich plagioclase; (4) growth of epidote and chlorite at the expense of plagioclase and clinopyroxene; and (5) sporadic growth of titanite (13P17).

We also analysed two fresh diorite samples for mineral chemistry. Diorites are equigranular and relatively fine-grained. Their mineralogy consists of plagioclase, amphibole, clinopyroxene, quartz, and accessory minerals including zircon, apatite, and undetermined oxides. Clinopyroxene occurs in 13P31, whereas amphibole is the only mafic mineral in 13P20. Oxides and zircon are present as accessory minerals. Epidote occurs as a secondary mineral in 13P20. Plagioclase in diorites is anhedral to subhedral; however, euhedral crystals are found within cm-sized plagioclase aggregates. Concentric zoning in plagioclase was rarely observed; most crystals are homogeneous, with anorthite contents of An_{40-45} ; thin (1–2 mm) sodic rims (as low as An_7) are common (Fig. 7c). Amphibole occurs as prismatic or anhedral crystals, testifying that it started to crystallize from the melt shortly before plagioclase. Amphiboles are Mg-hornblende but richer in Si and Mg with respect to amphiboles from gabbroic rocks (Fig. 7a). Similarly, to amphiboles from gabbros, amphiboles from quartz-diorites show a Amp_2 rims overgrowing Amp_1 magmatic cores. Amp_2 is richer in both Ti (0.10–0.18 apfu, atoms per formula unit) and Na (up to 0.31 apfu) with respect to Amp_1 (Table 2).

Table 2: Representative analyses of amphiboles from diorites, gabbros and amphibolites of the BSC.

alt-text: Table 2

Sample	13P20	13P20	13P20	13P23	TZ-3	TZ-3	13P23	13P23	13P17	13P17	13P17	13P17	13P17	13P17
Rock type	Qtz diorite	Qtz diorite	Qtz diorite	Gabbro	Gabbro	Gabbro	Gabbro	Gabbro	Amphib.	Amphib.	Amphib.	Amphib.	Amphib.	Amphib.
Mineral	Amp ₁	Amp ₁	Amp _{1 rim}	Amp ₁	Amp ₁	Amp ₁	Amp ₂	Amp ₂	Amp ₁	Amp ₁	Amp ₁	Amp ₂	Amp ₂	Amp ₂
SiO ₂	48.04	47.22	48.17	53.68	44.21	44.84	51.2	50.96	41	41.04	40.72	52.16	51.56	51.31
TiO ₂	0.77	1.3	1.06	0.33	2.54	2.57	1.2	0.95	1.81	1.91	1.77	0.13	0.13	0.08
Al ₂ O ₃	9.6	9.45	9.07	3.48	9.72	9.85	6.04	5.49	12.2	12.4	12.35	2.85	3.23	3.38
Cr ₂ O ₃	0.01	0.04	0.02	0.37	0.02	bd	0.17	0.12	0.05	bd	bd	bd	bd	0.04
Fe ₂ O ₃	nd	nd	nd	nd	nd	nd	nd	nd	3.03	3.39	3.15	2.88	3.71	4.04
FeO*	15.36	16.11	16.38	9.49	13.29	12.87	11.55	11.63	19	18.93	19.11	15.08	14.42	13.45
MnO	0.2	0.3	0.26	0.17	0.18	0.18	0.19	0.26	0.31	0.31	0.28	0.4	0.29	0.27
MgO	12.34	12.09	12.5	17.45	13.09	13.95	14.77	15.34	6.62	6.76	6.59	12.36	12.44	12.96
CaO	11.03	10.25	10.1	12.16	11.49	11.37	12.06	12.18	11.6	11.65	11.52	12.15	12.15	12.33
Na ₂ O	0.91	0.83	0.73	0.55	2.12	2.11	1.01	0.85	1.21	1.33	1.44	0.43	0.44	0.41
K ₂ O	0.28	0.34	0.34	0.09	0.41	0.34	0.21	0.17	1.75	1.84	1.8	0.2	0.22	0.2
Sum	98.55	97.93	98.62	97.77	97.08	98.13	98.41	97.95	98.6	99.56	98.74	98.63	98.59	98.48
Si	6.985	6.9374	7.0124	7.6363	6.5868	6.5766	7.376	7.3433	6.27	6.2173	6.2259	7.6052	7.5218	7.4757
Ti	0.0843	0.1441	0.1158	0.0355	0.2846	0.2835	0.1304	0.1026	0.21	0.2176	0.2035	0.0144	0.0148	0.0091
Al	1.6451	1.6363	1.5562	0.5835	1.7068	1.7027	1.0255	0.9324	2.19	2.214	2.2255	0.4898	0.5554	0.5804
Cr	0.001	0.0043	0.002	0.0415	0.0023	0	0.0198	0.0133	0.01	0	0.0005	0	0	0.0045
Fe ³⁺	0	0	0	0	0	0	0	0	0.35	0.3868	0.3629	0.3163	0.4074	0.4433
Fe ²⁺	1.8677	1.9794	1.9942	1.129	1.6559	1.5786	1.3915	1.4015	2.43	2.3979	2.4438	1.8383	1.7594	1.639
Mn	0.0243	0.0376	0.0317	0.021	0.0225	0.0222	0.0236	0.0317	0.04	0.04	0.0361	0.0499	0.0363	0.0334
Mg	2.6743	2.6475	2.7123	3.7	2.9069	3.0496	3.1715	3.2948	1.51	1.5264	1.5018	2.6861	2.705	2.8145
Ca	1.7183	1.6134	1.5753	1.8534	1.8342	1.7867	1.8615	1.8805	1.9	1.891	1.8872	1.8981	1.8991	1.9248
Na	0.2579	0.2365	0.2061	0.1509	0.6124	0.6	0.282	0.2378	0.36	0.3919	0.4269	0.1217	0.1256	0.1145
K	0.0529	0.0636	0.0623	0.0164	0.0787	0.0637	0.038	0.032	0.34	0.3556	0.3511	0.0369	0.0402	0.0379
Cations	15.311	15.3	15.268	15.167	15.691	15.664	15.32	15.27	15.6	15.638	15.665	15.057	15.065	15.077
xMg(Fe ²⁺)	0.589	0.572	0.576	0.766	0.637	0.659	0.695	0.702	0.38	0.389	0.381	0.594	0.606	0.632
xMg(Fe _{tot})	0.589	0.572	0.576	0.766	0.637	0.659	0.695	0.702	0.35	0.354	0.349	0.555	0.555	0.575

Na(M4)	0	0	0	0	0	0	0	0	0.1	0.109	0.113	0.102	0.101	0.075
Na(A)	0.258	0.237	0.206	0.151	0.612	0.6	0.282	0.238	0.26	0.283	0.314	0.02	0.025	0.039

$FeO^* = \text{total FeO as } Fe_2+$

Analyses of amphiboles from gabbros and diorites have been normalized considering 23 oxygens and 15 cations + Na + K; $Na(M4) = 0$.

Analyses of amphiboles from the 13P17 amphibolite have been normalized considering 23 oxygens and 13 cations Ca + K + Na; $(Mn, Fe(M4)) = 0$.

5.5 Whole rock geochemistry

Five samples of isotropic gabbros (TZ0, TZ3, 13P24, 13P25, 13P28) and one diorite (13P20) were analysed for bulk compositions (Table 4, Fig. 8). We also report (Table 4) a bulk-rock analysis of the dated sample (TZ1) of an aplitic dike, which we attribute to the Alichur granite.

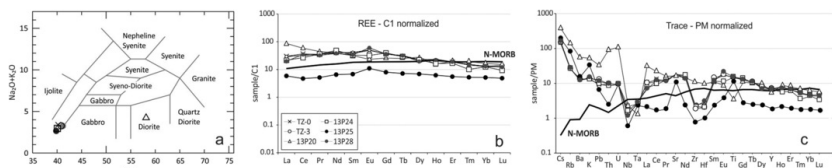


Figure 8. (a) Alkali-silica classification diagram (Cox et al., 1979) of intrusive rocks from the BSC. (b) Chondrite-normalized REE patterns of BSC rocks, chondritic values are after McDonough and Sun (1995). (c) Primitive Mantle (PM) normalized trace elements concentrations of BSC intrusive rocks. PM values are after McDonough and Sun (1995). The black pattern is representative of N-MORB basalts (Hofmann, 1988).

alt-text: Fig. 8

5.1.5.1 Methods

Whole rock analyses for major, minor and trace elements were determined by at the ACME Analytical Laboratories Ltd. in Vancouver (Canada). Total abundances of the major oxides were obtained by ICP-ES (Inductively Coupled Plasma Emission Spectroscopy), whereas REE (Rare Earth Element), refractory elements and precious and base metals by ICP-MS (Mass Spectroscopy). Sample preparations follow a $LiBO_2$ fusion and dilute nitric digestion for major oxides, REE and refractory elements, whereas precious and base metals were digested in aqua regia. Analytical errors are within 2% for major elements and in the 5% - 10% range for trace elements.

5.2.5.2 Results

The five gabbro samples have low Mg# (38-42, see Table 4) despite the very low SiO_2 content (41-43 wt% on anhydrous base), which suggests that they were derived from fairly evolved magmas. The non-primitive nature of gabbros of the Bashgumbaz Complex is also supported by the low Ni and Cr abundances (Table 4). Al_2O_3 positively correlates with SiO_2 and varies from 13.8 wt% for sample 13P25 (gabbro) to 17.5 wt% for sample 13P20 (diorite) (Table 4).

All samples display low primitive-mantle-normalized Nb, Ta, Zr and Hf abundances (Fig. 8c). Prominent peaks are observed in N-MORB/PM normalized patterns (McDonough and Sun, 1995) for Th and U of the quartz-diorite sample 13P20 and for Sr and Ti of the gabbro sample 13P25. The BSC samples are about 100 times richer in major lithophile elements and 10 times enriched in LREE (Fig. 8c) than N-MORB. The positive Ti peak in sample 13P25 is possibly related to the relatively high abundance of Ti-bearing phases (ilmenite and Ti-magnetite) in the measured sample and may not reflect the wider composition of the gabbroic body.

The chondrite-normalized REE patterns (Fig. 8b) differ slightly from one sample to another. Gabbro samples 13P24, 13P28, TZ0 and TZ3 show weak LREE enrichment ($\Sigma LREE = 53-58$) with respect to HREE ($\Sigma HREE = 20-12$, Table 4), with $(La/Yb)_N$ between 2.33 and 2.50 and small positive Eu anomalies ($Eu/Eu^* = 1.31-1.73$). Samples from these gabbros have 20-30 times chondritic values (Fig. 8b) and are slightly enriched in LREE with respect to N-MORB, whereas HREE values closely match N-MORB ones.

Gabbro sample 13P25 has the lowest REE concentrations among the analysed samples, with values even lower than N-MORB, with no relative enrichment between LREE and HREE and a small positive Eu anomaly ($Eu/Eu^* = 1.50$).

Quartz diorite sample 13P20 is the most REE-enriched, with a small fractionation between LREE ($\Sigma LREE = 119$) and HREE ($\Sigma HREE = 87$). A negative Eu anomaly ($Eu/Eu^* = 0.60$) likely reflects plagioclase fractionation during magma evolution.

6.6 Geochronology

We use U-Pb zircon dating and amphibole ^{40}Ar - ^{39}Ar dating **from** of intrusive rocks **off** from the gabbro-serpentinite unit to constrain the timing of development of the Bashgumbaz complex. Zircon grains were **analyzed** **analysed** in situ by means of LA-MC-ICPMS after careful characterization of zircon crystals via optical microscopy and cathodoluminescence imaging to identify inclusions and zoning domains within each grain. Amphiboles **s** samples (ca. 3–5 mg) were **analyzed** **analysed** by stepwise heating.

6.1-6.1 Methods

Zircon U, Th, and Pb isotopes were measured at the Arizona Laserchron Center (ALC). For sample 13P20, zircon was dated in-situ in two thin sections of the sample. For sample 13P21, zircon grains were separated using standard mineral-separation techniques, mounted in epoxy and polished. A Nu Plasma LA-MC-ICPMS was used for sample 13P21, utilizing Faraday detectors for ^{238}U , ^{232}Th , ^{208}Pb , ^{207}Pb and ^{206}Pb and discrete-dynode ion counters for ^{204}Pb and ^{202}Hg with a 30 μm ablation-pit diameter (“Faraday” analyses). To resolve consistent-age domains in small grains (20–50 μm wide) with improved spatial resolution in-situ in two thin sections of sample 13P20, a 15 μm ablation-pit diameter was used with Faraday collectors for ^{238}U and ^{232}Th and ion counters for all Pb isotopes (“ion-counter” analyses). Cathodoluminescence images were used to ensure that ablation pits did not overlap multiple age domains or inclusions. Data reduction (including common-Pb correction) was performed using the Excel macro *AGECALC.XLS* (Gehrels et al., 2008) and ALC web site (<http://www.laserchron.org>) for further analytical details. We used *Isoplot* (Ludwig, 2008) to calculate crystallization ages, using only 80–105%-concordant analyses ($^{206}\text{Pb}/^{238}\text{U}$ / $^{206}\text{Pb}/^{207}\text{Pb}$) for which $^{206}\text{Pb}/^{238}\text{U}$ and $^{206}\text{Pb}/^{207}\text{Pb}$ uncertainty > 10%.

TZ3 gabbro sample was crushed and sieved to extract the 250–500 μm fraction. After magnetic separation of an amphibole-rich separate, individual grains were hand-picked under a binocular microscope. Selected grains were then cleaned ultrasonically in deionized water and then wrapped in aluminium foil. Sample and age monitors were irradiated at the Triga Mark II reactor at the University of Pavia (Italy).

Stepwise heating experiments were performed at the Department of Earth and Environmental Sciences of the University of Milano Bicocca (Italy) following the protocol by Villa et al. (2000), using the following interference corrections: $(^{39}\text{Ar}/^{37}\text{Ar})_{\text{Ca}} = 0.00067$; $(^{36}\text{Ar}/^{37}\text{Ar})_{\text{Ca}} = 0.000255$; $(^{40}\text{Ar}/^{39}\text{Ar})_{\text{K}} = 0.033$. Samples were loaded in a double vacuum resistance furnace and heated in 10 steps for about 20 **minutes** **min** at temperatures from 500°C to 1400°C. The released gas was transferred to a tandem of two hot and cold SAES™ Zr-Al getter pumps, cleaned for ca. 15 min, and introduced into a Nu Instruments Noblesse™ rare gas mass spectrometer. The five Ar isotopes were measured in one Faraday cup and one ion counter in peak jumping mode. Analytical data of $^{40}\text{Ar}/^{39}\text{Ar}$ stepwise-heating experiments are reported in Table 3 after machine background and ^{37}Ar decay corrections only. Age **were** **was** recalculated relative to a MMhb-1 age of 523.1 Ma (Renne et al., 1998).

Table 3-Table 3 Representative analyses of olivine, clinopyroxene and plagioclase from diorites, gabbros and amphibolites of the BSC.

alt-text: Table 3

Sample	13P23	13P23		13P23	13P23	TZ-3	TZ-3		13P24	TZ-3	13P20	13P17	13P17
Rock type	Ol-gabbro	Ol-gabbro		Ol-gabbro	Ol-gabbro	Gabbro	Gabbro		Gabbro	Gabbro	Diorite	Amphib.	Amphib.
Mineral	Ol	Ol		Cpx	Cpx	Cpx	Cpx		Pl	Pl	Pl	Pl ₁	Pl ₂
SiO ₂	39.63	39.18		52.13	52.82	52.56	52.35		51.04	51.81	67.2	60.44	66.67
TiO ₂	0.03	0.09		0.27	0.29	0.22	0.37		0.06	0.02	0	0	0.02
Al ₂ O ₃	0	0		2.6	2.11	1.5	1.66		31.27	30.38	21.21	25.49	21.08
Cr ₂ O ₃	0.03	0.05		0.44	0.36	0.04	0		0.07	0.01	0.01	0	0
Fe ₂ O ₃				1.34	0.64	1.91	1.45		0	0.29	0	0	0.12
FeO*	15.98	17.18		5.24	5.45	7.01	8.31		0.24	0	0.03	0.07	0
MnO	0.18	0.24		0.24	0.25	0.3	0.36		0	0	0	0.02	0.03
MgO	43.96	42.49		15.09	14.83	14.56	14.42		0.02	0	0	0.02	0
CaO	0.08	0.15		22.23	23.72	21.91	21.02		13.64	13.09	1.46	6.85	1.63

Na ₂ O	0	0		0.36	0.18	0.36	0.35		3.61	4.1	10	7.67	11.02
K ₂ O	0	0		0.02	0.02	0.01	0		0.07	0.1	0.23	0.25	0.15
Sum	99.89	99.38		99.94	100.66	100.4	100.3		100.02	99.81	100.13	100.8	100.72
Si	1.0007	1.0016		1.9243	1.9392	1.947	1.9457		2.3217	2.3559	2.9611	2.6718	2.6718
Ti	0.0006	0.0017		0.0074	0.008	0.0062	0.0104		0.0019	0.0007	0	0	0
Al	0	0		0.1131	0.0913	0.0655	0.0726		1.6764	1.6281	1.1015	1.328	1.328
Cr	0.0006	0.001		0.0127	0.0104	0.0012	0		0.0025	0.0003	0.0004	0	0
Fe ³⁺	nd	nd		0.0372	0.0177	0.0532	0.0405		0	0.01	0	0	0
Fe ²⁺	0.3375	0.3673		0.1619	0.1674	0.2172	0.2582		0.0093	0	0.001	0.0026	0.0026
Mn	0.0039	0.0052		0.0075	0.0076	0.0095	0.0114		0	0	0	0.0006	0.0006
Mg	1.6546	1.619		0.8303	0.8115	0.8039	0.7988		0.0013	0.0002	0	0.0012	0.0012
Ca	0.0022	0.0041		0.8792	0.933	0.8696	0.8371		0.6648	0.6377	0.0689	0.3244	0.3244
Na	0	0		0.0255	0.0128	0.0259	0.0252		0.3184	0.3615	0.8544	0.6574	0.6574
K	0	0		0.001	0.001	0.0006	0.0001		0.0038	0.0056	0.0127	0.014	0.014
Cations	3.0001	2.9999		4.0001	3.9999	3.9998	4		5	5	5	5	5
xMg(Fe ²⁺)	0.828	0.81	xMg(Fe ²⁺)	0.837	0.829	0.787	0.756	An	0.674	0.635	0.389	0.326	0.075
Forsterite	0.828	0.811	Wo	0.405	0.44	0.411	0.397	Ab	0.323	0.36	0.354	0.66	0.917
Fayalite	0.169	0.184	En	0.415	0.406	0.402	0.399	Or	0.004	0.006	0.109	0.014	0.008
			CaTiAl ₂ O ₆	0.007	0.008	0.006	0.01						

FeO*_T = total FeO as Fe₂O₃. Ab_T

Analyses of olivines have been normalized on the basis of 4 oxygens and 3 cations. Pyroxene analyses have been normalised on the basis of 6 oxygens and 4 cations.

Analyses of plagioclase have been normalised on the basis of 8 oxygens and 5 cations (Ab: albite; An: ~~anortithe~~anorthite; Or: orthoclase).

Table 4. Whole rock chemical analyses of rocks from the Bashgumbaz Complex.

alt-text: Table 4

	Bashgumbaz Complex						Alichur granite
	TZ0	TZ3	13P20	13P24	13P25	13P28	TZ1
SiO ₂ (wt%)	40.24	40.85	58.14	40.07	39.84	41.20	67.63
TiO ₂	3.19	3.05	0.74	3.17	2.42	3.21	0.40
Al ₂ O ₃	16.22	16.68	17.46	16.19	13.76	16.56	12.38
Cr ₂ O ₃	<0.002	<0.002	<0.002	<0.002	<0.002	<0.002	bd
Fe ₂ O ₃	14.41	15.15	6.77	15.78	21.74	14.78	3.02

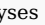
MgO	4.97	4.82	3.33	5.78	7.13	4.89	1.24
MnO	0.19	0.18	0.13	0.20	0.23	0.18	0.06
CaO	9.94	9.28	7.24	9.74	9.93	9.34	5.00
Na ₂ O	2.82	2.85	2.66	2.56	1.67	2.80	5.64
K ₂ O	0.42	0.41	1.59	0.39	0.98	0.45	0.12
P ₂ O ₅	1.93	2.09	0.26	1.87	0.01	1.93	0.40
LOI	5.50	4.40	1.54	3.80	1.90	4.20	4.10
Total	99.81	99.79	99.86	99.55	99.61	99.54	99.94
Anhydrous							
SiO ₂ (wt%)	43.32	43.53	59.54	42.55	41.70	43.90	70.75
TiO ₂	3.43	3.25	0.76	3.37	2.53	3.42	0.42
Al ₂ O ₃	17.46	17.77	17.88	17.19	14.40	17.64	12.95
FeO _t	13.96	14.53	6.24	15.08	20.48	14.17	2.84
MgO	5.35	5.14	3.41	6.14	7.46	5.21	1.30
MnO	0.20	0.19	0.13	0.21	0.24	0.19	0.06
CaO	10.70	9.89	7.41	10.34	10.39	9.95	5.23
Na ₂ O	3.04	3.04	2.72	2.72	1.75	2.98	5.90
K ₂ O	0.45	0.44	1.63	0.41	1.03	0.48	0.13
P ₂ O ₅	2.08	2.23	0.27	1.99	0.01	2.06	0.42
Total	100.00	100.00	100.00	100.00	100.00	100.00	100.00
<i>Mg#</i>	<i>40.59</i>	<i>38.66</i>	<i>49.35</i>	<i>42.05</i>	<i>39.38</i>	<i>39.59</i>	<i>44.85</i>
Ba (ppm)	85	89	385	78	104.00	83	52
Rb	17.1	16.4	89	16.3	50.1	17.3	4.3
Sr	383.1	383.9	340	378	255.5	382.9	345.3
Co	28.8	30.4	14	29.78	68.6	29.07	5.6
Ga	15.4	19.5	9.7	15.3	17.0	17.2	11
Nb	1.5	0.9	4.3	1.1	<0.1	0.8	6.4
Ni	0.3	0.3	2.3	0.3	0.1	0.3	4.6
Pb	1.4	2	5.2	1.5	1	1.8	3.4
Sc	30	30	18	29	61	29	7
Th	0.8	0.8	7.6	0.7	0.2	0.8	4.1
U	0.2	0.2	2.3	0.2	0.2	0.2	2.8

V	248	278	bd	256	309	265	42
Zr	26.5	20.6	120	24.3	8.6	24.5	58.1
Y	30.4	31.8	24.3	29.8	8.5	30.8	13.7
Hf	0.8	0.6	2.9	0.6	0.3	0.9	1.8
Ta	0.2	0.45	1.2	0.2	0.13	0.11	1.1
Cs	3.1	3.2	8.4	3.3	4.2	3.5	0.5
La	7.1	6.9	21	7	1.4	6.9	7.2
Ce	22.5	19.7	38	16.5	2.9	21.3	16.9
Pr	3.24	3.28	4.25	3.33	0.48	3.25	1.87
Nd	20.1	18	19	22.2	3	17.4	7.7
Sm	5.59	6.08	4.7	4.88	1.01	5.02	1.91
Eu	2.74	2.84	1.4	1.8	0.62	3.4	0.56
Gd	7.3	7.22	10.8	7.87	1.59	7.21	2.03
Tb	1.08	1.14	1.7	1.07	0.26	1.15	0.4
Dy	5.48	5.66	8.52	5.51	1.7	4.78	2.35
Ho	1.1	1.24	1.66	0.89	0.34	1.21	0.48
Er	3.01	3.01	3.92	3.01	0.89	3.03	1.39
Tm	0.36	0.38	0.62	0.25	0.13	0.36	0.2
Yb	2.05	2.12	2.87	2.01	0.83	2.09	1.49
Lu	0.31	0.34	0.4	0.23	0.12	0.3	0.22
ΣREE	81.96	77.91	118.84	76.55	15.27	77.40	44.70
ΣLREE	58.53	53.96	86.95	53.91	8.79	53.87	35.58
ΣHREE	20.69	21.11	30.49	20.84	5.86	20.13	8.56
Eu/Eu*	1.31	1.31	0.60	0.89	1.50	1.73	0.87
(La/Yb) _n	2.48	2.33	5.25	2.50	1.21	2.37	3.47
(La/Sm) _n	0.82	0.73	2.88	0.93	0.89	0.89	2.43
(Gd/Yb) _n	6.30	6.18	1.87	5.96	3.95	7.81	2.32

LOI - Loss On ignition; FeO* - total Fe expressed as $FeO^* = 0.8998 \cdot Fe_2O_3$; Mg# = molar $MgO / (MgO + FeO^*) \cdot 100$; bd - below detection limit; ΣREE - rare earth element sum; n subscript - normalization to chondrite values; ΣLREE - light rare earth element sum; ΣHREE - heavy rare earth element sum; (Sun and McDonough, 1989); $Eu/Eu^* = Eu_n / RADQ(Sm_n \cdot Gd_n)$.

Table 5. Zircon U-Pb results.

alt-text: Table 5

Sample-analysis #	U (ppm)	²⁰⁶ Pb ²⁰⁴ Pb	U/Th	Th/U	Isotopic ratios							Apparent ages (Ma)						6867C (%)	6875C (%)
					²⁰⁶ Pb* ²⁰⁷ Pb*	1σ (%)	²⁰⁷ Pb* ²³⁵ U*	1σ (%)	²⁰⁶ Pb* ²³⁸ U	1σ (%)	Error corr.	²⁰⁶ Pb* ²³⁸ U*	1σ (Ma)	²⁰⁷ Pb* ²³⁵ U	1σ (Ma)	²⁰⁶ Pb* ²⁰⁷ Pb*	1σ (Ma)		
<i>Sample 13P20, diorite from the GSU</i>																			
n = 3 analyses: Concordia age = 221.8 ± 3.8 Ma; ²⁰⁶ Pb/ ²³⁸ U weighted-mean age = 221.6 ± 3.8 Ma																			
13P20a-Z28-1	144	9236	1.9	0.51	19.7406	1.4	0.2413	1.7	0.0345	1.1	0.61	218.9	2.3	219.5	3.4	225.3	31.8	97%	100%
13P20a-Z15-2	181	15121	2.8	0.36	19.3700	2.3	0.2503	2.5	0.0352	1.0	0.41	222.8	2.2	226.8	5.0	268.9	51.8	83%	98%
13P20a-Z18-1	209	19799	2.2	0.46	19.5452	1.2	0.2489	1.7	0.0353	1.2	0.71	223.5	2.6	225.7	3.4	248.2	27.6	90%	99%
n = 15  227-245 Ma analyses																			
13P20a-Z25-1	186	23522	2.0	0.51	19.8076	0.9	0.2498	1.2	0.0359	0.8	0.67	227.2	1.8	226.4	2.4	217.4	20.6	105%	100%
13P20a-Z32-1	144	18953	1.7	0.57	19.6373	1.3	0.2522	1.7	0.0359	1.0	0.60	227.5	2.2	228.3	3.4	237.3	30.8	96%	100%
13P20a-Z17-2	393	57193	3.8	0.26	19.5011	0.8	0.2588	1.3	0.0366	0.9	0.74	231.7	2.1	233.7	2.6	253.4	19.3	91%	99%
13P20b-Z12-2	272	28345	7.2	0.14	19.4321	1.2	0.2603	1.9	0.0367	1.5	0.78	232.3	3.5	234.9	4.1	261.5	27.7	89%	99%
13P20b-Z6-1	272	90417	6.5	0.15	19.6788	0.8	0.2574	2.1	0.0367	1.9	0.91	232.5	4.3	232.5	4.3	232.5	19.5	100%	100%
13P20b-Z7-1	225	30595	1.7	0.57	19.7434	1.7	0.2591	1.9	0.0371	1.0	0.50	234.8	2.2	233.9	4.0	224.9	38.3	104%	100%
13P20b-Z9-1	113	18520	2.0	0.50	19.7453	2.2	0.2595	2.9	0.0372	1.9	0.66	235.2	4.3	234.2	6.0	224.7	50.0	105%	100%
13P20b-Z10-1	2316	424919	3.8	0.27	19.4866	0.5	0.2637	2.0	0.0373	1.9	0.96	235.9	4.5	237.7	4.2	255.1	12.2	92%	99%
13P20b-Z11-1	134	25407	1.5	0.68	19.5161	0.9	0.2643	2.4	0.0374	2.2	0.93	236.8	5.1	238.1	5.0	251.7	20.1	94%	99%
13P20b-Z8-1	156	37084	2.2	0.46	19.5689	1.1	0.2674	2.7	0.0380	2.4	0.92	240.2	5.8	240.6	5.7	245.4	24.6	98%	100%
13P20b-Z7-2	143	26371	1.8	0.57	19.4090	1.7	0.2704	2.1	0.0381	1.2	0.57	240.8	2.8	243.0	4.5	264.3	39.3	91%	99%
13P20b-Z13-1	90	17549	1.8	0.55	19.4305	2.3	0.2701	3.5	0.0381	2.6	0.75	240.8	6.2	242.8	7.6	261.8	53.5	92%	99%
13P20a-Z13-2	87	6266	1.9	0.51	19.6429	3.3	0.2675	3.4	0.0381	0.3	0.08	241.1	0.7	240.7	7.2	236.7	77.0	102%	100%
13P20b-Z4-1	189	45660	4.8	0.21	19.4927	0.8	0.2727	1.3	0.0386	1.0	0.78	243.9	2.5	244.8	2.9	254.4	19.2	96%	100%
13P20a-Z19A-1	179	16209	1.4	0.69	19.5668	1.2	0.2732	1.8	0.0388	1.3	0.72	245.2	3.0	245.3	3.8	245.7	28.3	100%	100%
<i>Sample 13P21, Bashgumbez Bashqumbaz granite</i>																			
n = 14 analyses: Concordia age = 117.5 ± 1.4 Ma; ²⁰⁶ Pb/ ²³⁸ U weighted-mean age = 117.3 ± 1.5 Ma																			
13P21b-26	1120	9306	1.9	0.53	20.6861	3.5	0.1193	3.9	0.0179	1.6	0.42	114.4	1.8	114.4	4.2	116.0	83.1	99%	100%
13P21b-10	1105	35948	1.7	0.59	20.6980	2.7	0.1216	2.8	0.0182	0.7	0.26	116.6	0.8	116.5	3.1	114.6	64.4	102%	100%
13P21b-25	1878	109545	5.0	0.20	20.3856	1.4	0.1238	1.8	0.0183	1.0	0.59	116.9	1.2	118.5	2.0	150.4	33.3	78%	99%
13P21b-21	1373	108339	1.6	0.62	20.4921	2.6	0.1233	2.9	0.0183	1.3	0.45	117.0	1.5	118.0	3.3	138.2	61.9	85%	99%
13P21b-28	1327	32459	3.4	0.30	20.5773	1.6	0.1228	2.5	0.0183	1.9	0.76	117.0	2.2	117.6	2.7	128.5	37.9	91%	100%

13P21b-23	1143	89.925	5.1	0.20	20.5091	3.1	0.1232	4.9	0.0183	3.8	0.78	117.1	4.4	118.0	5.5	136.2	72.9	86%	99%
13P21b-12	1489	37.561	19.5	0.05	20.7436	2.0	0.1219	2.6	0.0183	1.7	0.65	117.1	2.0	116.8	2.9	109.4	47.2	107%	100%
13P21b-17	583	12.817	1.5	0.66	20.4973	6.2	0.1236	6.6	0.0184	2.2	0.33	117.4	2.5	118.4	7.4	137.6	146.4	85%	99%
13P21a-03	860	80.780	2.8	0.36	20.5203	1.7	0.1247	4.3	0.0186	4.0	0.92	118.5	4.7	119.3	4.9	135.0	39.7	88%	99%
13P21b-27	447	15.123	1.8	0.55	20.6371	8.7	0.1247	12.3	0.0187	8.7	0.71	119.2	10.3	119.3	13.8	121.6	204.3	98%	100%
13P21b-30	1657	84.530	23.5	0.04	20.6139	1.9	0.1252	2.3	0.0187	1.4	0.58	119.6	1.6	119.8	2.6	124.2	44.3	96%	100%
13P21a-05	1038	47.550	4.0	0.25	20.6505	1.9	0.1265	2.5	0.0189	1.6	0.65	121.0	1.9	121.0	2.8	120.1	44.0	101%	100%
13P21a-06	1095	63.748	1.5	0.66	20.5547	1.0	0.1319	2.8	0.0197	2.6	0.93	125.6	3.2	125.8	3.3	131.1	24.1	96%	100%

Table 6. Analytical results of Ar-Ar dating of amphibole, sample TZ3. 6867C and 6875C are the concordances of the $^{206}\text{Pb}/^{238}\text{U}$ and $^{207}\text{Pb}/^{206}\text{Pb}$ ages, and the $^{206}\text{Pb}/^{238}\text{U}$ and $^{207}\text{Pb}/^{235}\text{U}$ ages, respectively.

alt-text: Table 6

T (°C)	^{40}Ar total	Err. ^{40}Ar	^{39}Ar	Err. ^{39}Ar	% ^{39}Ar	^{38}Ar	Err. ^{38}Ar	$^{38}\text{Ar}/\text{Cl}$	^{37}Ar	Err. ^{37}Ar	^{36}Ar	Err. ^{36}Ar	Age	Error age	Ca/K	Error Ca/K	Cl/K	Error Cl/K
800	4.63E-08	2.86E-11	1.75E-11	3.64E-13	14.57356	6.38E-11	8.54E-14	3.54E-11	9.98E-11	9.04E-13	1.49E-10	3.38E-13	165.29	10.57	11.11	0.25	0.36	0.01
875	2.92E-09	4.16E-13	7.44E-12	3.38E-13	6.198504	2.93E-12	7.83E-15	1.49E-12	4.31E-11	8.87E-13	7.12E-12	1.87E-14	177.44	8.18	11.28	0.56	0.04	0.00
960	4.55E-09	8.58E-13	1.74E-11	3.9E-13	14.49584	4.74E-12	9.03E-15	2.79E-12	1.13E-10	9.07E-13	9.16E-12	2.38E-14	174.55	3.98	12.65	0.30	0.03	0.00
1015	4.63E-09	1.01E-12	1.38E-11	4.16E-13	11.5225	5.83E-12	1.06E-14	3.68E-12	1.33E-10	9.15E-13	1.04E-11	2.59E-14	185.77	5.70	18.81	0.58	0.05	0.00
1045	3.1E-09	7.54E-13	1.26E-11	4.16E-13	10.48405	4.19E-12	9.61E-15	2.7E-12	4.51E-11	8.87E-13	7.09E-12	1.9E-14	131.53	4.42	6.97	0.27	0.04	0.00
1095	3.93E-09	9.88E-13	1.2E-11	4.41E-13	9.975836	5.62E-12	1.11E-14	3.77E-12	8.06E-11	8.97E-13	9.01E-12	2.29E-14	173.74	6.51	13.12	0.51	0.06	0.00
1145	5.29E-09	1.17E-12	1.51E-11	3.38E-13	12.62	6.75E-12	1.24E-14	4.31E-12	1.43E-10	9.19E-13	1.18E-11	2.97E-14	193.05	4.44	18.45	0.43	0.05	0.00
1200	8.59E-09	1.79E-12	1.11E-11	4.41E-13	9.218302	8.59E-12	1.39E-14	3.93E-12	1.74E-10	9.34E-13	2.38E-11	5.52E-14	223.43	9.34	30.78	1.25	0.06	0.00
1255	5.5E-09	1.14E-12	6.46E-12	3.64E-13	5.38322	4.99E-12	1E-14	1.93E-12	9.58E-11	9E-13	1.57E-11	3.82E-14	208.52	12.21	29.06	1.67	0.05	0.00
1345	4.3E-09	9.88E-13	6.64E-12	3.12E-13	5.528178	4.72E-12	9.66E-15	2.45E-12	1.2E-10	9.1E-13	1.15E-11	2.84E-14	219.13	10.63	35.60	1.71	0.07	0.00

Sample weight = 0.00987 g. J = 0.000965. All data are in mL. Errors are 1σ .

6.2.6.2 U/Pb zircon dating

Analyzed/Analysed zircon grains from the 13P20 quartz-diorite are ca. 20-50 μm in size (Fig. 9c), they occur as slightly elongated to equant subhedral prisms with aspect ratios of 1:2 to 1:3. Most zircon crystals display a typical oscillatory growth zoning, with alternate bright and dark rims ranging from sub-micrometric to several μm in thickness.

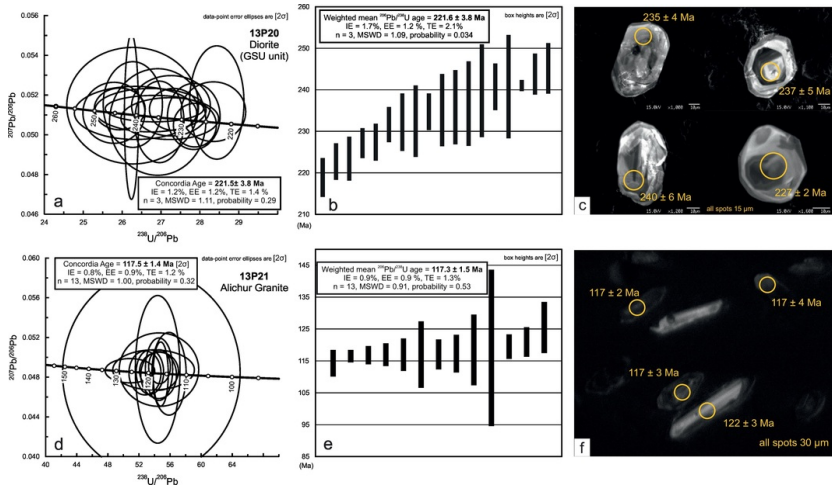


Figure 9. Zircon U-Pb results for samples 13P20 and 13P21. (a) Tera-Wasserburg concordia diagram of 13P20 diorite from the GSU unit. The youngest statistically meaningful age is obtained from three analyses showing a 221.6 ± 3.8 Ma concordia age. (b) Corresponding weighted-mean $^{206}\text{Pb}/^{238}\text{U}$ ages of the aforementioned concordant zircon analyses. (c) Cathodoluminescence images of representative zircon crystals analysed for U-Pb dating. (d) Tera-Wasserburg concordia diagram of cross-cutting Alichur granite sample 13P21 (which intruded the BSC), showing a 117 ± 2 Ma concordia age for a population of 13 concordant analyses. (e) Corresponding weighted-mean $^{206}\text{Pb}/^{238}\text{U}$ age of sample 13P20 based on 13 analyses. (f) Cathodoluminescence images of representative zircon crystals analysed for U-Pb dating. MSWD: Mean Square of Weighted Deviates.

alt-text: Fig. 9

A few crystals are texturally different and show a patchy complex zoning, which appears to overprint and partially replace oscillatory growth zoning. These crystals have ages in the lower range of the measured interval (Table 5). Inclusions of apatite and rutile are common, and occur generally close to the cores of zircon crystals. Most zircon grains exhibit slightly rounded rims, which may derive both from partial resorption due to a change in Zr saturation in the magma during the final crystallization stage, and by corrosion by aggressive hydrothermal solutions. This textural variability attests a complex magmatic evolution for zircon of gabbros and diorites of BSU. In this scenario, U-Pb zircon ages could not be simply interpreted as crystallization ages, but they record a complex history of antecrystic zircon crystallization, re-equilibration, and resorption, which occurred within the magmatic plumbing system of the Bashgumbaz arc. The interval in obtained ages on different zircon grains (Fig. 9b) ranges from ca. 240 Ma to ca. 220 Ma, testifying to a 20 Ma long history of zircon growth and re-equilibration. Th/U ratios (Table 5) of analyzed analysed zircon grains range up to 0.70 supporting the magmatic origin of each dated zircon grain.

U-Pb zircon concordant ages of the GSU diorite sample 13P20 show no clear relationships with zircon grains textural domains (Figure 9a, b; Table 5). We thus suggest that the youngest statistically meaningful age (221.6 ± 3.8 Ma, Table 5) could be considered as the minimum crystallization age of intermediate intrusive member of the BSC.

Analyzed analysed zircon grains from granitoid sample 13P21 are more elongated and somewhat larger (30–70 μm), and display typical igneous oscillatory growth zoning (Fig. 9f). Some inherited cores occur within a few zircon grains (Fig. 9c). For Alichur granite sample 13P21, 13 concordant analyses produced similar, $117 \text{ Ma} \pm 2 \text{ Ma}$ concordia and $^{206}\text{Pb}/^{238}\text{U}$ weighted-mean ages that we interpret to reflect granite crystallization (Figure 9d, e; Table 5).

The Cretaceous age suggests that the Alichur granite is one of the northernmost manifestation of the subduction-related magmatism that characterized the Andean-type margin of southern Eurasia from 130 Ma to Eocene times (Heuberger et al., 2007; Chapman et al., 2018) after the Karakoram and Kohistan accretion.

6.3.6.3 $^{40}\text{Ar}/^{39}\text{Ar}$ amphibole dating

We dated relict magmatic amphibole by the $^{40}\text{Ar}/^{39}\text{Ar}$ stepwise heating method to further constrain the intrusion age of the Bashgumbaz gabbros. Isotropic gabbros of the GSU, even outside shear zones, are partially retrogressed (see Section 4), with green actinolitic amphibole and chlorite that substitute brown magmatic hornblende (Fig. 10a). Petrographic analyses showed that magmatic texture and mineral assemblage are least retrogressed in sample TZ3, where the primary magmatic composition is preserved at least within amphibole cores.

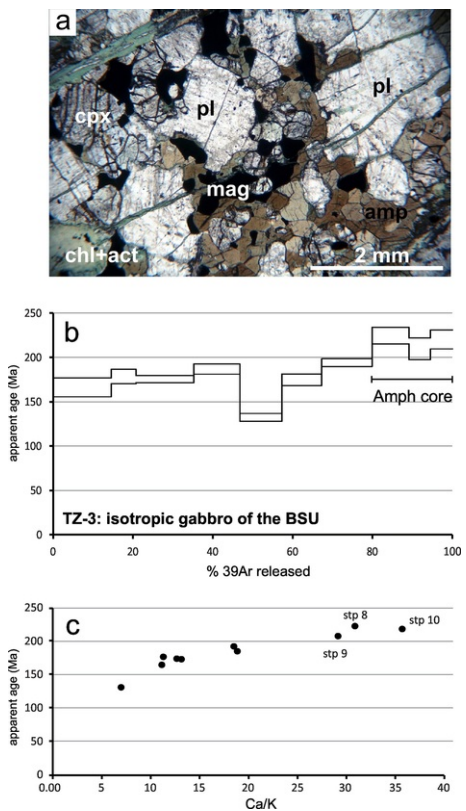


Figure 10. (a) Microstructure and mineral phase assemblage of the TZ3 isotropic gabbro. The magmatic texture is still largely preserved, but retrogression of the primary magmatic hornblende is indicated by the growth of actinolite-chlorite aggregates. (b) Spectrum of the cumulative ^{39}Ar release during the step-heating experiment: highlighted steps ("Amph core") correspond to gas release by hornblende cores as suggested by Ca/K ratios (c) Three-isotope correlation diagram ($^{40}\text{Ar}/^{39}\text{Ar}$ vs. $^{37}\text{Ar}/^{39}\text{Ar}$) scaled to give step age as a function of step Ca/K. The roughly linear correlation is evidence of a mainly binary mixing between magmatic hornblende, constrained to be 218 ± 12 Ma old on the basis of the match between step Ca/K and EPMA analyses, and a secondary retrogression phase, constrained to be ≤ 127 Ma old.

alt-text: Fig. 10

^{40}Ar - ^{39}Ar stepwise heating on the TZ3 amphibole separate yielded a discordant age spectrum (Table 6, Fig. 10b). This is the typical behaviour observed for mineral mixtures (Müller et al., 2002) and predicted for TZ3 by the petrographical evidence of a retrogressed hornblende. The combination of the isotope composition of released Ar and the minerochemical data obtained with EPMA analyses allows to correlate each degassing step with the corresponding compositional domains of the degassing mineral (e.g. Villa et al., 2000; Allaz et al., 2011). We note that step ages correlate with the Ca/K ratios (calculated from the measured $^{37}\text{Ar}/^{39}\text{Ar}$) of the respective steps (Fig. 10c). This correlation is broadly linear, which means that the mineral separate predominantly consists of two K reservoirs (Villa, 2001). The reservoir degassed at high furnace temperatures can be easily identified by its chemical fingerprint: steps 8, 9, and 10 have Ca/K ratios between 29 and 35 (Table 6, Fig. 10c), identical to the interval measured by EPMA in texturally well identified hornblende cores, Ca/K = 28–33 (Table 2 and Fig. 7a and 7b). The "isochemical" age (sensu Villa et al., 2006) of the three steps that correspond to the hornblende cores is 218 ± 12 Ma, indistinguishable from the zircon age of diorite 13P20 from the Gabbro-Serpentine Unit. The agreement between these two chronometers is a robust evidence that the magmatic age of the whole BSEGSU is ca. 222 Ma.

Identifying the secondary phase having low Ca/K ratios is less straightforward. It is not actinolite, which always has very low K concentrations, very high Ca/K ratios, and could not account for about half of the total K mass balance of the sample. A typical K-rich secondary hydrothermal mineral could be alkali feldspar (adularia ± albite) or its degradation product, sericite. Because the K concentration of both alkali feldspar and sericite can be 50 times higher than that of amphibole, it is sufficient that the volume fraction of this secondary phase be 1% to actually control the first half of the age spectrum. The comparatively low Cl/K ratio of the young, low-temperature steps supports the suggestion of feldspar as an important contaminant. Irrespective of its true mineralogical identity, this secondary phase has an age constrained by the lower end of the correlation trend in Fig. 10c. As the step with the lowest Ca/K

ratio has a step age of 127 ± 9 Ma (95% confidence level), it follows that sample TZ3 also records a ~~hydrothermal~~ hydrothermal reaction event at $t \leq 127$ Ma. The coincidence of this age with the U-Pb age of the Alichur granite sample 13P21, 117 ± 2 Ma, is evidence that magmatism was the thermal engine for the hydrothermal circulation in the BSC at ca. 117 Ma.

7.7 Origin of the BSC and its geodynamic significance

7.1.7.1 Permian-Mesozoic palaeogeographic setting and position of the BSC

The provenance and geodynamic significance of the BSC requires understanding of a wider geological context than the SE Pamir. We summarize here the main geological features of the surrounding blocks.

7.1.1.7.1.1 The Rushan-Pshart Zone

This complex tectonic sector, now consisting of a Cenozoic belt of imbricates with serpentinite-bearing tectonic slivers, was considered by [Dronov \(1964\)](#) as a zone distinct from both Central and SE Pamir, as it is characterized by a significant Permian rifting-related basaltic volcanism ([Shvol'man and Pashkov, 1986](#)). This Permian basin closed during the Jurassic or the Cretaceous ([Schwab et al., 2004](#); [Robinson, 2015](#) and references therein). Faunal affinities between Central and SE Pamir suggest that the Rushan basin was relatively small. [Leven \(1995\)](#) recognizes four different tectonic blocks: Rushan, West Pshart, East Pshart and Dunkeldyk.

The Rushan Zone consists of a thick, likely Carboniferous to Triassic, mixed terrigenous to carbonate succession that rests unconformably upon a low-grade metamorphic basement made of mica schists and phyllite. Felsic tuffs occur in the upper part of the section. According to [Leven \(1995\)](#), this block has no features in common with the surrounding units and should be considered distinctly.

The Pshart block includes the West and East Pshart zones. The West Pshart shows a thick succession of Lower Permian fusulinid limestones interbedded with picritic basalts, interpreted as an expression of continental rifting ([Leven, 1995](#)). Basalts and andesitic basalts with intermediate and acidic tuffs occur in the intermediate part of the succession, which passes up-section to a thick unit containing volcanoclastic sandstones and shales of undetermined Mesozoic age.

The East Pshart zone succession starts with a thick terrigenous unit of middle Carboniferous to ?Early Permian age followed by Upper Permian volcanoclastic limestones with basalts. The Triassic interval consists of ~~more than~~ ≥ 1000 m of Upper Triassic volcanic deposits (Gumbezkol Group) overlying Lower to Middle Triassic cherts, shales, sandstones with andesite and basalt layers. Coral assemblages found in blocks contained within lavas at the base of the Gumbezkol Group indicate an early Carnian age, whereas its upper part, mainly consisting of andesitic products, is considered Late Triassic. Mixed terrigenous volcanic units tentatively dated to the Jurassic and Early Cretaceous occur in a higher stratigraphic position ([Leven, 1995](#)).

The Dunkeldyk block also includes two distinct portions. The northern part is correlative with the West Pshart Zone, as the southern part is similar to the East Pshart block and is correlative with its Permian-Triassic part.

Based on these features, [Leven \(1995\)](#) argued that rifting occurred in between the West and East Pshart zones, and not between the East Pshart and SE Pamir as previously suggested ([Pashkov and Shvol'man, 1979](#); [Pashkov and Budanov, 1990](#)). The West Pshart zone more closely resembles the Central Pamir due the characters and stratigraphic position of the Permian carbonates, which may represent part of a single shallow-sea carbonate platform that continuously developed from ~~the Sakmarian~~ ~~to for most of~~ the Permian ([Leven, 1993](#)). On the other hand, the East Pshart Zone and SE Pamir show common features especially for the Permian part of the succession and for the occurrence of volcanic rocks within the Upper Permian beds. An apparent difference between the two blocks is the occurrence of thick Upper Triassic volcanic deposits in the East Pshart Zone, which are generally absent in the internal units of the SE Pamir. However, [Leven \(1995\)](#) described Triassic volcano-sedimentary successions associated with Ladinian-Carnian coral limestones in the peripheral northern and eastern distal part of SE Pamir ([Dronov, 1988](#)), which suggests that the two areas were originally continuous during the Triassic.

7.1.2.7.1.2 The Central Pamir

This strongly deformed and metamorphosed terrane possibly consists of different blocks ([Schwab et al., 2004](#)). The southern one, the Kalaktash block, shows the lower Palaeozoic Sarez Formation, which is unconformably followed by ?Upper Carboniferous-Lower Permian sandstones and limestones. These are in turn unconformably overlain by Middle to Upper Permian carbonates, followed up section by Lower and Middle Triassic marine deposits with bauxite layers at the base. The Permian succession includes well-dated fossiliferous carbonate beds ([Leven, 1993](#)), which indicate a warmer ~~climate during the~~ Asselian-Sakmarian ~~climate~~ than that in the SE Pamir, where the thick terrigenous deposits of the Bazardara Group were being deposited. Upper Triassic fine-grained continental to shallow sea terrigenous deposits with sporadic conglomerates at the top of the Vomar Formation rest on older units and are followed up-section by Jurassic limestones without any evident unconformity. Nevertheless, the collision of the Central and North Pamir ~~with the emergence of the region~~, following the final closure of the Palaeotethys suture ([Robinson et al., 2012](#)), is documented by the Triassic age of metamorphic zircons from the Muztaghata Dome. Here, high-grade metasediments of the Central Pamir are juxtaposed to metamorphic fragments of the Karakul Mazar terrane, which is part of the North Pamir, resting in a lower structural position ([Robinson et al., 2012](#)).

7.2.7.2 The Bashgumbaz Complex as a remnant of a magmatic arc

The association of ultramafic/mafic rocks in the BSC led geologists ([Pashkov and Shvol'man, 1979](#); [Shvol'man, 1978, 1980](#)) to interpret it as an ophiolitic complex. However, rather than strictly representing mid-ocean ridges, ophiolites exhibit a wide range of variable features that likely indicate various geodynamic settings including supra-subduction environments (SSZ ophiolites of [Pearce et al., 1984](#); [Pearce, 2003](#)), back-arc basins, mantle plumes and forearcs ([Whattam, 2009](#); [Whattam and Stern, 2011](#); [Dilek and Furnes, 2014](#)).

Mantle-derived rocks, mafic intrusive rocks, and basaltic lavas all occur within the BSC, but conclusive field relationships that can be used to infer that they are parts of a primitive rock association are lacking. The basalts of the Chatyrtash Group (Shvol'man, 1980) are consistently in tectonic contact with gabbros of the GSU and they did not experience the same tectonometamorphic evolution of the GSU rocks. The Chatyrtash basalts are mostly non-metamorphosed and non-deformed, apart from shear zones developed at the contact with other units of the BSC. Conversely, harzburgites, gabbros and diorites of the GSU are all internally deformed and variably affected by low-grade metamorphism.

Moreover, because no evidence of a sheeted-dike complex that could relate the GSU to the Chatyrtash basalts has been reported, a typical MORB ophiolitic sequence cannot be documented in the BSC.

Gabbros of the GSU are commonly associated with more highly differentiated magmas such as diorites and quartz-diorites. Ubiquitous amphibole as a mafic phase within these mafic and intermediate rocks indicates a significant involvement of hydrothermal fluids in the magma genesis. This indicates a subduction-related setting for the genesis of the parent magmas of gabbros and diorites of the BSC. The relatively low Mg# of the GSU gabbros indicate that the Bashgumbaz gabbros crystallized from a fairly evolved magma. These ~~feature~~features, together with high LILE contents, Nb-Ta negative anomalies, and relatively high fractionation of LREE with respect to HREE (Fig. 8b, and 8c), suggest a subduction-related setting for the genesis and emplacement of the Bashgumbaz magmatic rocks.

The serpentized harzburgites and the gabbroic rocks of the GSU do not preserve their original relationships, as shear zones invariably occur along the contacts. The association of an exhumed and serpentized mantle with intrusive rocks that display geochemical features typical of a supra-subduction zone setting could be either explained as an ophiolite formed in the fore-arc region of a relatively old subduction zone or as a tectonic assemblage of rock units that are not genetically related. Volcanic and intrusive rocks with a calc-alkaline and/or boninitic affinity are reported from many Tethyan ophiolites (e.g. Dilek and Furnes, 2014) and are interpreted to represent pieces of the fore-arc lithosphere formed after a certain time interval, necessary for the subducting oceanic crust to progressively hydrate and metasomatize the above mantle wedge, after subduction initiation (Whattam and Stern, 2011). In most cases, arc-like rocks occur within ophiolitic complexes together with lavas and intrusives of MORB- and IAT-like affinity (e.g. Shervais et al., 2004). A chemostratigraphic evolution, from MORB-like to VAB-like lavas is commonly observed and interpreted to ~~reflects~~reflect the compositional change in the mantle source as partial melting and subduction-related metasomatic processes go on (Whattam and Stern, 2011).

Gabbros and diorites of the GSU occur instead alone, with no other associated volcanic or intrusive rocks of different geochemical affinity. In addition, the metasedimentary rocks of the MSU could not be directly considered the metamorphic sole of an ophiolitic complex, as they lack the typical high-grade metamorphism (Wakabayashi and Dilek, 2000, 2003). Despite the intense deformation that affected mica schists and quartzites of the MSU under greenschist facies conditions, relicts of a pre-existing phase assemblage are still observable as partly chloritized garnets and biotites, suggesting that peak conditions experienced by the MSU rocks have not exceeded those of the lower amphibolite facies. The only clue that could support the interpretation of the Bashgumbaz complex as an ophiolite is the occurrence of serpentinites. However, as no crosscutting relationships have been observed with magmatic rocks, the serpentized harzburgites of the GSU should be considered as a separate tectonic slice that has been tectonically coupled to other units during underthrusting and exhumation processes related to the Cimmerian collision.

7.3.7.3 The Cimmerian Collisions, the closure of the Rushan Ocean and the emplacement of the Bashgumbaz Complex

Several lines of evidence, including radiometric dating and stratigraphic constraints, indicate that the Palaeotethys suture zone between the Karakul-Mazar arc and the Central Pamir terrane sutured around 200 Ma (Robinson, 2015). In the SE Pamir, two lines of evidence indicate the occurrence of an important Cimmerian orogenic event: (i) a syn-orogenic Upper Triassic flysch sequence (Dronov, 2006; Angiolini et al., 2015); (ii) the unconformity between the lowermost Jurassic deposits and intensively deformed Permian-Triassic units.

The Cimmerian structures trend roughly N-S and are exposed to the north of Bashgumbaz. This belt is clearly overprinted by Mesozoic-Cenozoic E-W-trending fold-and-thrust systems. Based on available data, the suggested collision age of SE Pamir with Central Pamir is bracketed between the Middle Triassic and earliest Jurassic (Vlasov et al., 1991; Dronov and Leven, 1990; Dronov et al., 2006; Angiolini et al., 2013a, 2015).

Notwithstanding the complex Cenozoic tectonics, which significantly reworked the Mesozoic structures, most authors believe that the emplacement of the BSC occurred during the Late Triassic (Shvol'man and Pashkov, 1986; Burtman and Molnar, 1993; Schwab et al., 2004). Thick Upper Triassic volcanic products in the East-Pshart Zone and in the northern external portions of the ~~South-East~~SE Pamir provide evidence of an active volcanic arc during this time interval. Stratigraphic affinities between the Permian-Triassic successions from the two blocks also imply that they were contiguous and located along the same side of the Rushan-Pshart Ocean. Our data show that the intrusive component of the BSC may represent the root of the arc, which formed in response to southward subduction and consequently developed along the southern margin of the Rushan-Pshart Ocean (Fig. 11). The petrographic composition of the lowermost Jurassic red clastic deposits, which are widespread in the ~~South-East~~SE Pamir, also testify to the erosion of a magmatic arc located in a proximal position, rather than sourcing from the suture zone between Central and North Pamir as suggested by Robinson (2015).

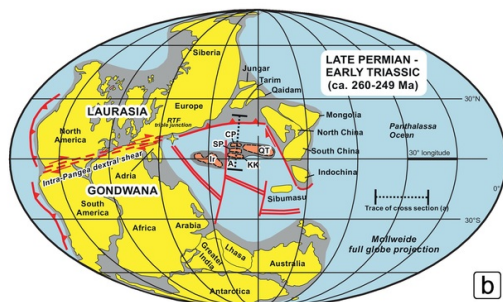
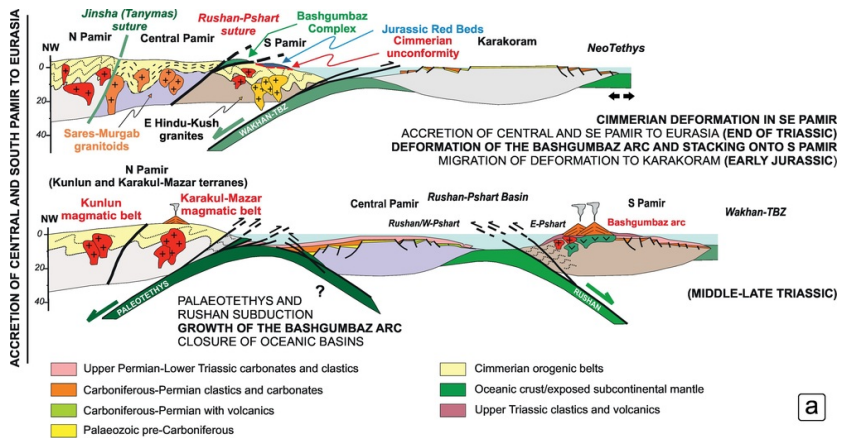


Figure 11- Fig. 11 (a) Cartoon depicting the tectonic evolution of the accretion of the Central and South Pamir to Eurasia, in response of the closure of the Palaeotethys ocean and the Rushan basin (modified after Angiolini et al., 2013a, 2013b). (b) Palaeogeographic reconstruction of the Palaeotethys realm at the Permian-Triassic transition. Central Pamir and South Pamir are separated by the Rushan basin (Fig. 11a), the Wakhan basin divides South Pamir from Karakoram and Afghanistan blocks (modified after Angiolini et al., 2015). A: Afghanistan; CP: Central Pamir; Ir: Iran; KK: Karakoram; QT: Qiantang; SP: South Pamir.

alt-text: Fig. 11

In its present-day structural position, the BSC (Fig. 3) occurs in the hangingwall side of both the Alichur detachment and the normal fault that bounds the complex on the north flank of the Alichur valley. The BSC is thus sandwiched in between the Alichur Dome and the Tashdzhilga Group. Like the Tashdzhilga flysch, the BSC could had been originally close to the Rushan-Pshart zone, and transported southward during the Cimmerian collision.

The Tashdzhilga Group olistoliths appear to have a dual origin, some being derived from the Central Pamir-West Pshart Zone and others from the East Pshart Zones. The relation with the Central Pamir is indicated by the occurrence of carbonate olistoliths with Lower Permian fusulinid associations. Sedimentation in Central Pamir was characterized by the development of carbonate platforms with fusulinids due to their northern latitude with and warmer marine waters. In contrast, the sedimentation in the East Pshart Zone, SE Pamir and Karakoram is predominantly represented by the cold water terrigenous facies of the Bazardara Group and correlative units (Angiolini et al., 2007). However, the occurrence of reworked blocks of acidic lavas, volcanoclastic sandstones within the matrix of the olistoliths and Carnian corals that are similar to those documented in the Gumbekol Group of the East Pshart Zone, indicate that also this area was a possible source for the olistostromes.

Olistostromic units (Doradek and Urushdzhilgatash formations) similar to the Tashdzhilga Group occur in the Northern Alichur Range north of Bashgumbaz village in a complex structural setting, forming a flysch succession that may correlate with the Upper Triassic terrigenous units of the SE Pamir. In addition, here olistoliths comprise volcanic rocks and upper Palaeozoic carbonate blocks, suggesting a wide regional distribution for these peculiar deposits (Dronov et al., 1989). Ages obtained from microfaunas identified in the blocks range from Late Carboniferous to Middle Permian. The oldest faunas, as well as most of the foraminifer assemblages, suggest that their source is external to the SE Pamir, but still of uncertain origin. However, no clear affinity with Central Pamir has been established (Dronov et al., 1989). An additional question concerns the mechanism that emplaced these large, reworked carbonate blocks into a clastic, fine-grained unit. The textural character of the Tashdzhilga unit, which comprises abundant exotic rock fragments of different age and composition embedded in a volcanoclastic sandy-silty matrix, is typical of an active collisional margin and resembles a sub-nappe olistostrome (e.g., Festa et al., 2016). These deposits, which possibly formed precursor olistostromes, correspond to Mutti et al.'s (2009) "wildflysch" and are generally deposited in

migrating foredeep basins in front of advancing thrust sheets and nappes (Fig. 12a), which subsequently assimilate them into the orogen (Fig. 12b). A similar hypothesis was proposed for the origin of the olistostromes present in the Upper Triassic North Alichur series (Dronov et al., 1989). The same authors indicate a possible pre-Rhaetian time for their deposition and subsequent tectonic emplacement.

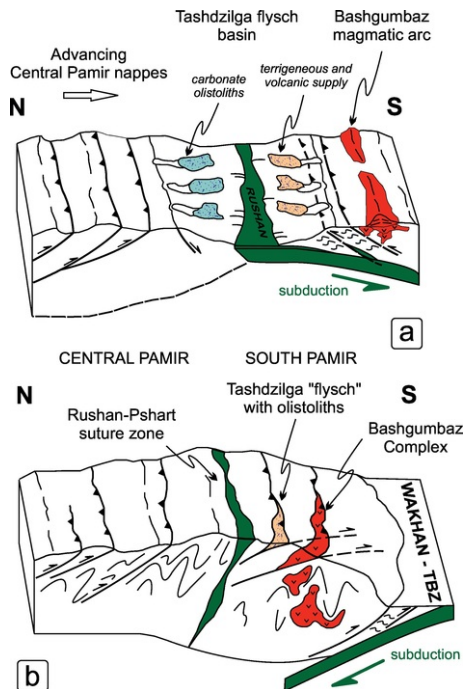


Figure 12: Fig. 12 (a) Conceptual model of the formation of the Tashdzhilga olistostromes. Flyschoid sediments come from both the advancing Central Pamir nappes and the Bashgumbaz magmatic arc. The features of the Tashdzhilga olistostromes and enclosing flysch matrix suggest that they developed as sub-nappe olistostrome (Festa et al., 2016), typical of collisional setting with ongoing oceanic subduction. (b) After the continental collision between Central Pamir and South Pamir, the Bashgumbaz Complex and the Tashdzhilga flysch unit were involved in the south-verging nappe stack of SE Pamir.

alt-text: Fig. 12

We suggest that the Tashdzhilga and possibly also the North Alichur olistostromes formed within the external portion of the Late Triassic SE Pamir foredeep during the closure of the Ruhan-Pshart basin, when the Central Pamir was thrust over the East Pshart block and the SE Pamir in a post-collisional setting (Figs. 11 and 12). Advancing carbonate nappes, including Permian limestones, fed the olistostrome deposition into the basin. Obduction of the Central Pamir also triggered the overthrusting of the deep portion of the beheaded arc and its obduction onto the SE Pamir, forming the Bashgumbaz Complex. Final telescoping of the SE Pamir foredeep and out-of-sequence thrusting may account for the present-day upper structural position of the Tashdzhilga Group with respect to the arc-related units.

In this model, Jurassic magmatism and Late Jurassic radiometric ages obtained in the Rushan-Pshart Zone (Schwab et al., 2004) likely indicate the protraction of deformation in a post-collisional setting, as also proposed by Robinson (2015).

7.4.7.4 Regional correlations of the Pamir suture zones

The main Palaeotethys suture of the Pamir, which now corresponds to the Tanyas Thrust Zone (Fig. 13), was previously correlated to the Jinsha Suture of Tibet, which was interpreted in the past to represent the closure of the major subduction zone between the Cimmerian blocks and the southern margin of Eurasia during the Late Triassic (Burtman and Molnar, 1993; Schwab et al., 2004). Recent reconstructions of the geodynamic evolution of Tibet, however, indicate that the main Palaeotethys suture corresponds to the Longu Co-Shuanghu Suture (Fig. 13), which bisects the Qiangtang block (Zhao et al., 2015). This suture zone, which also closed during the Late Triassic, juxtaposes the Cathaysian North Qiangtang Terrane and the Gondwanan South Qiangtang Terrane, which represent two blocks with different palaeogeographic affinities and evolutions (Zhao et al., 2015). However, contrasting evidence found in the

western Tibetan Plateau led some authors (Jolivet, 2017 and references therein for a review) to claim for the existence of a single Qiangtang Block. In this view, the mélangé units exposed in the central part of the block are considered as subduction-eroded rocks that have been off scraped from the Jinsha suture, and then underthrust beneath the Qiangtang Block.

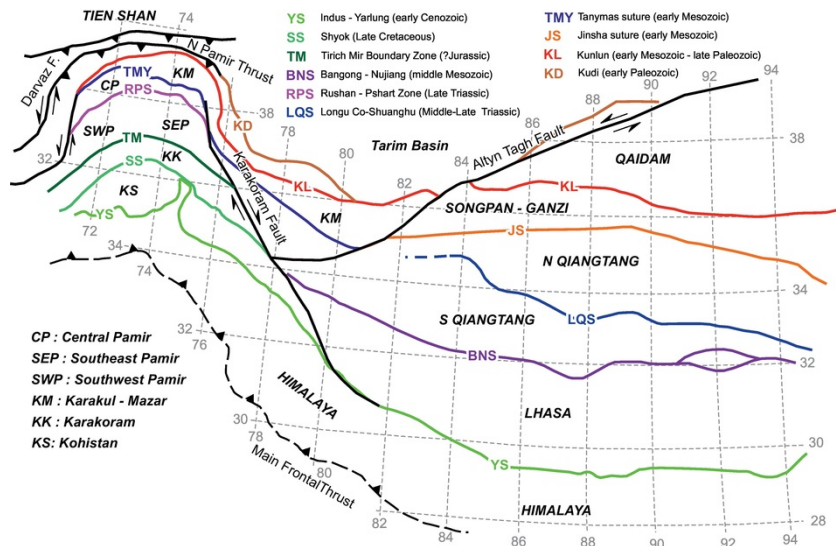


Figure 13. Fig. 13 Tectonic scheme of the Pamir-Karakoram-Himalaya-Tibet area with indicated the main suture zones, based on data from Burtman and Molnar (1993), Yin and Harrison (2000), and Schwab et al. (2004). The location of the Tirich Mir Boundary Zone is after Zanchi et al. (2000); the trace of the Longu Co-Shuanghu suture in the Qiangtang block is from Zhao et al. (2015) and Zhang et al. (2015).

alt-text: Fig. 13

The Jinsha Suture, which is located to the north of the North Qiangtang terrane, is interpreted as a secondary suture that likely represents the late Triassic closure of a back-arc basin (Zhang et al., 2015). Based on this interpretation, the Rushan-Pshart Suture is a regional tectonic feature, as it does not correlate with the Longu Co-Shuanghu Suture (as tentatively suggested by Angiolini et al., 2013a, 2013b), nor with the Mesozoic Bangong-Nujiang suture (between the South Qiangtang and the Northern Lhasa terranes, e.g. Liu et al., 2017). As a consequence, the correlation across the Karakoram Fault between the Central Pamir-North Qiangtang block and the South Pamir-South Qiangtang block is not straightforward, contrary to what proposed by Yang et al. (2017). The correlation of the Rushan-Pshart with Mesozoic sutures in the Afghan area is also problematic. Looking at the southern boundary of South Pamir, the scenario is even more complex. Here, the Tirich Mir Boundary Zone marks the pre-mid-Cretaceous accretion of the Karakoram block to South Pamir and East Hindu Kush (Zanchi et al., 2000; Heuberger et al., 2007). This suture zone does not correlate with any other east of the Karakoram Fault (Fig. 13), pointing again to a lateral heterogeneity of the southern Eurasia margin during the Mesozoic.

Even if regional correlations are always intriguing, we should consider that the internal fragmentation of the composite Karakoram, South Pamir and Central Pamir microplate may be a peculiar feature of this complex terrane.

The occurrence of intervening basins that never evolved into oceanic spreading centres (Zanchi and Gaetani, 1994, 2011; Angiolini et al., 2013a, 2013b) testifies for the likely absence of direct correlations with major suture zones in the Himalaya and Tibetan plateau.

8.8 Conclusions

Petrographic and geochemical data suggest that magmatic intrusive rocks of the Bashgumbaz Complex formed in a supra-subduction-zone setting along the southern margin of the Rushan-Pshart Ocean, in close relations with the East Pshart zone of Leven (1995). Subduction-related magmatism occurred at least until the lower Norian, as indicated by the ca. 222 Ma crystallization age of a diorite belonging to the Gabbro-Serpentinites unit of the complex.

The deformation and low-grade metamorphism of the Bashgumbaz Complex can be bracketed in time between the Late Triassic (youngest age of magmatic rocks) and the deposition of the lowermost Jurassic strata of the Darbasatash Group above the Cimmerian unconformity. The complex was then intruded by the Cretaceous (117 Ma) Alichur granite.

We suggest that the Bashgumbaz Complex was initially underthrust and then obducted onto the southern margin of the closing Rushan Ocean, together with fragments of the Central Pamir sedimentary cover. The

metamorphism and deformation that affected the Bashgumbaz Complex thus represents a time-marker for the accretion of the South Pamir terrane to the Eurasia margin.

In this framework, the Rushan-Pshart Suture does not correlate with any sutures along-strike to the west (Hindu Kush and Afghanistan Mesozoic sutures) or to the east (Tibet). Neither the Longu Co-Shuanghu nor the Bangong-Nuhjiang sutures can be considered as correlative with the Rushan-Pshart as they differ both in structural position and supposed time of ocean closure.

Uncited references

[Dilek and Furnes, 2009](#)

[Irvine and Baragar, 1971](#)

[Jin, 2002](#)

[Li et al., 2006](#)

[Ritter, 1987](#)

[Wetherill, 1956](#)

[Yang et al., 2011](#)

[Zhang et al., 2010](#)

[Zhang et al., 2013](#)

Acknowledgements

Field work and analytical data of this research were funded by the DARIUS PROGRAMME, Project CA11/01 and by [SF Tectonics grant EAR-1419748](#), [NSF Tectonics grant EAR-1419748](#) and [NSF Instrumentation & Facilities grant EAR-1338583](#). Detailed reviews by J. Wakabayashi, S.A. Whattam and two anonymous reviewers helped us to ameliorate a first version of the paper. T Tsunogae is kindly acknowledged for the editorial handling of the paper. [Our Tajik colleagues A. Niyazov and J. Mamadjanov are thanked for permissions and for introducing us to the Bashgumbaz area.](#)

References

Angiolini L., Gaetani M., Muttoni G., Stephenson M.H. and Zanchi A., Tethyan oceanic currents and climate gradients 300 m.y. ago, *Geology* **35**, 2007, 1071-1074.

Angiolini L., Zanchi A., Zanchetta S., Nicora A. and Vezzoli G., The Cimmerian geopuzzle: new data from South Pamir, *Terra Nova* **25**, 2013a, 352-360.

Angiolini L., Crippa G., Muttoni G. and Pignatti J., Guadalupian (Middle Permian) paleobiogeography of the Neotethys Ocean, *Gondwana Research* **24**, 2013b, 173-184.

Angiolini L., Zanchi A., Zanchetta S., Nicora A., Vuolo I., Berra F., Henderson C., Malaspina N., Rettori R. and Vezzoli G., From rift to drift in South Pamir (Tajikistan): Permian evolution of a Cimmerian terrane, *Journal of Asian Earth Sciences* **102**, 2015, 146-169.

Angiolini L., Campagna M., Borlenghi L., Grunt T., Vachard D., Vezzoli G., Vuolo I., Worthington J., Nicora A. and Zanchi A., Brachiopods from the Cisuralian-Guadalupian of Darvaz, Tajikistan and implications for Permian stratigraphic correlations, *Palaeoworld* **25**, 2016, 539-568.

Bard J.P., Metamorphism of an obducted island-arc: example of the Kohistan sequence (Pakistan) in the Himalayan collided range, *Earth and Planetary Science Letters* **65**, 1983, 133-144.

Burtman V.S., Tien Shan, Pamir, and Tibet: **H**istory and **G**eodynamics of Phanerozoic **O**ceanic **B**asins, *Geotectonics* **44** (5), 2010, 388-404.

Burtman V.S. and Molnar P., Geological and **G**eophysical **E**vidence for **D**eeper **S**ubduction of **C**ontinental **C**rust **B**eneath the Pamir, In: *Geological Society of America Special Paper 281*, 1993, 76.

Coward M.P., Butler R.W.H., Khan M.A. and Knipe R.J., The tectonic history of Kohistan and its implications for Himalayan structure, *Journal of the Geological Society* **144**, 1987, 377-391.

Cox K.G., Bell J.D. and Pankhurst R.J., *The Interpretation of Igneous Rocks*, 1979, Allen and Unwin; London, (450 pp).

- Davydov V.I., Komissarova R.A., Khranov A.N. and Chediya I.O., Paleomagnetism of upper Permian rocks of the Southeastern Pamir, *Doklady Akademii Nauk SSSR* **267**, 1982, 1177-1181.
- Dilek Y. and Furnes H., Structure and geochemistry of Tethyan ophiolites and their petrogenesis in subduction rollback systems, *Lithos* **113**, 2009, 1-20.
- Dilek Y. and Furnes H., Ophiolites and their origins, *Elements* **10** (2), 2014, 93-100.
- Dronov V.I., On the south boundary of Central Pamir, *Materialy po geologii Pamira* **2**, 1964, 133-137, (in Russian).
- Dronov V.I., The stratigraphy of pre-Jurassic (P-T) volcano-sedimentary beds in the Bashgumbez, Irikjak, Sedek and Tash Djilga valleys (South-East Pamir), *Akad. Nauk. Tadjik. SSR Doklady Akademii Nauk Tadjikskoi SSR Doklady* **29** (9), 1986, 549-552, (in Russian).
- Dronov V.I., The volcanogeneous type of the Triassic deposits of the South-East Pamir (Katta Mardjanay river basin), *Akad. Nauk. Tadjik. SSR Doklady Akademii Nauk Tadjikskoi SSR Doklady* **303** (2), 1988, 437-439, (in Russian).
- Dronov V.L. and Leven E.Ja., Age of carbonate conglomerates of the central zone of SE Pamir, *Doklady Akademii Nauk Tadjik SSR Doklady Akademii Nauk Tadjikskoi SSR* **25**, 1990, 232-235, (in Russian).
- Dronov V.L., Melnikova G.K., Salibajev G.C., Bardashev I.A., Minajiev V.E. and Muchabatov M.M., Stratigraphic dictionary of the Pamir, 2006, Technische Universität Bergakademie Freiberg, 252.
- Faisal S., Larson K.P., King J. and Cottle J.M., Rifting, subduction and collisional records from pluton petrogenesis and geochronology in the Hindu Kush, NW Pakistan, *Gondwana Research* **35**, 2016, 286-304.
- Festa A., Ogata K., Pini G., Dilek Y. and Alonso J.L., Origin and significance of olistostromes in the evolution of orogenic belts: A global synthesis, *Gondwana Research* **39**, 2016, 180-203.
- Gehrels G.E., Valencia V. and Ruiz J., Enhanced precision, accuracy, efficiency, and spatial resolution of U-Pb ages by laser ablation-multicollector-inductively coupled plasma-mass spectrometry, *Geochemistry, Geophysics, Geosystems* **9**, 2008, , Q03017 <https://doi.org/10.1029/2007GC001805>.
- Hofmann A.W., Chemical differentiation of the Earth: the relationship between mantle, continental crust and oceanic crust, *Earth and Planetary Science Letters* **90**, 1988, 297-314.
- Irvine F.N.T.N. and Baragar W.R.A.W.R.A., A guide to the chemical classification of the common volcanic rocks, *Canadian Journal of Earth Sciences* **8**, 1971, 523-548.
- Jin X.X., Permo-Carboniferous sequences of Gondwana affinity in southwest China and the paleogeographic implications, *Journal of Asian Earth Sciences* **20**, 2002, 633-646.
- Jolivet M., Mesozoic tectonic and topographic evolution of Central Asia and Tibet: a preliminary synthesis, In: Brunet M.F., McCann T. and Sobel E.R., (Eds.), *Geological Evolution of Central Asian Basins and the Western Tien Shan Range*, *Geological Society of London Special Publications* vol. **427**, 2017, 19-55.
- Leven E.J., Main events in the Permian History of the Tethys and Fusulinids, *Stratigr. Geol. Correlations Stratigraphy and Geological Correlation* **1**, 1993, 59-75.
- Leven E.J., Permian and Triassic of the Rushan-Pshart Zone (Pamir), *Rivista Italiana di Paleontologia e Stratigrafia* **101**, 1995, 3-16.
- Li C., Zhai Q., Dong Y. and Huang X., Discovery of eclogite and its geological significance in Qiangtang area, central Tibet, *Chinese Science Bulletin* **51**, 2006, 1095-1100.
- Liang X., Wang G., Yuan G. and Liu Y., Structural sequence and geochronology of the Qomo Ri accretionary complex, Central Qiangtang, Tibet: Implications for the Late Triassic subduction of the Paleo-Tethys Ocean, *Gondwana Research* **2282**, 2012, 470-481.
- Liu Y., Santosh M., Zhao Z., Niu W.C. and Wang G.H., Evidence for palaeo-Tethyan oceanic subduction within central Qiangtang, northern Tibet, *Lithos* **127**, 2011, 39-53.
- Liu D., Shi R., Ding L., Huang Q., Zhang X., Yue Y. and Zhang L., Zircon U-Pb age and Hf isotopic compositions of Mesozoic granitoids in southern Qiangtang, Tibet: Implications for the subduction of the Bangong-Nuijiang Tethyan Ocean, *Gondwana Research* **41**, 2017, 157-172.
- Ludwig K.R., Isoplot 3.6. Berkeley Geochronology Center Special Publications 4, 2008, (77 pp).
- McDonough W.F. and Sun S.S., Composition of the Earth, *Chemical Geology* **120**, 1995, 223-253.
- Müller W., Kelley S.P. and Villa I.M., Dating fault-generated pseudotachylytes: comparison of ⁴⁰Ar/³⁹Ar stepwise-heating, laser ablation and Rb-Sr microsampling analyses, *Contributions to Mineralogy and Petrology* **144**, 2002, 57-77.

- Mutti E., Bernoulli D., Ricci Lucchi F. and Tinterri R., Turbidites and turbidity currents from Alpine 'flysch' to the exploration of continental margins, *Sedimentology* **56**, 2009, 267-318.
- Novikov P., Titan-bearing Upper Permian Volcano-sedimentary Formation in South-East Pamir, 1979, Geological prospecting Institute, 1-23, (Thesis, in Russian).
- Pashkov B.R. and Budanov V.I., Tectonics of the SW-SE Pamir junction, *Geotectonics* **24**, 1990, 246-253.
- Pashkov B.R. and Shvolman V.A., Rift margins of Tethys in the Pamir, *Geotectonics* **13** (6), 1979, 447-456.
- Pearce J.A., Supra-subduction zone ophiolites: the search for modern analogues, In: Dilek Y. and Newcomb S., (Eds.), *Ophiolite Concept and the Evolution of the Geological Thought, Geological Society of America Special Paper* **vol. 373**, 2003, 269-293.
- Pearce J.A., Harris N.B.W. and Tindle A.G., Trace element discrimination diagrams for the tectonic interpretation of granitic rocks, *Journal of Petrology* **25**, 1984, 956-983.
- Renne P.R., Swisher C.C., Deino A.L., Karner D.B., Owens T.L. and DePaolo D.J., Intercalibration of standards, absolute ages and uncertainties in $^{40}\text{Ar}/^{39}\text{Ar}$ dating, *Chemical Geology* **145**, 1998, 117-152.
- Ritter S.M., Biofacies-based refinement of Early Permian conodont biostratigraphy, in central and western USA, In: Austin R.A., (Ed), *Conodonts - Investigative Techniques and Applications, British Micropalaeontological Society Series* 1987, Ellis Horwood Ltd.; Chichester, England, 382-403.
- Robinson A.C., Mesozoic tectonics of the Gondwanan terranes of the Pamir plateau, *Journal of Asian Earth Sciences* **102**, 2015, 170-179.
- Robinson A.C., Ducea M. and Lapen T.J., Detrital zircon and isotopic constraints on the crustal architecture and tectonic evolution of the northeastern Pamir, *Tectonics* **31**, 2012, <https://doi.org/10.1029/2011TC003013>.
- Schmidt J., Hacker B.R., Ratschbacher L., Stübner K., Stearns M., Kylander-Clark A., Cottle J.M., Alexander A., Webb G., Gehrels G. and Minaev V., Cenozoic deep crust in the Pamir, *Earth and Planetary Science Letters* **312**, 2011, 411-421.
- Schwab M., Ratschbacher L., Siebel W., McWilliams M., Minaev V., Lutkov V., Chen F., Stanek K., Nelson B., Frisch W. and Wooden J.L., Assembly of the Pamir: Age and origin of magmatic belts from the southern Tien Shan to the southern Pamir and their relation to Tibet, *Tectonics* **23**, 2004, [TC4002https://doi.org/10.1029/2003TC001583](https://doi.org/10.1029/2003TC001583).
- Şengör A.M.C., Natalin B.A. and Burtman V.S., Evolution of the Altaid tectonic collage and Palaeozoic crustal growth in Eurasia, *Nature* **364**, 1993, 299-307.
- Shervais J.W., Kimbrough D.L., Renne P., Hanan B.B., Murchey B., Snow C.A., Zoglman Schuman M.M. and Beaman J., Multi-stage origin of the Coast Range Ophiolite, California: implications for the life cycle of supra-subduction zone ophiolites, *International Geology Review* **46**, 2004, 289-315.
- Shvolman V.A., Relicts of the Mesotethys in the Pamir, *Himalayan Geology* **8**, 1978, 369-378.
- Shvolman V.A., Mesozoic ophiolites in the Pamir, *Geotectonics* **14** (6), 1980, 465-470.
- Shvolman V.A. and Pashkov B.R., Early Cretaceous tectonic zonation of central Asia, *Dokl. Akad. Nauk SSSR Doklady Akademii Nauk SSSR* **286** (4), 1986, 951-954, (in Russian).
- Stampfli G.M. and Pillevuit A., An alternative Permian-Triassic reconstruction of the kinematics of the Tethyan realm, In: *Atlas Tethys Palaeoenvironmental Maps. Explanatory Notes*, 1993, 55-62.
- Stübner K., Ratschbacher L., Rutte D., Stanek K., Minaev V., Wiesinger M., Gloaguen R. and Project TIPAGE members, The giant Shakh dara migmatitic gneiss dome, Pamir, India-Asia collision zone: 1. Geometry and kinematics *Tectonics* **32**, 2013a, 948-979, <https://doi.org/10.1002/tect.20057>, (2013).
- Stübner K., Ratschbacher, Weise C., Chow J., Hofmann J., Khan J., Rutte D., Sperner B., Pfander J., Hacker B.R., Dunkl I., Tichomirowa M., Stearns M.A. and Project TIPAGE members, The giant Shakh dara migmatitic gneiss dome, Pamir, India-Asia collision zone: 2. Timing of dome formation, *Tectonics* **32**, 2013b, 1404-1431, <https://doi.org/10.1002/tect.20059>, (2013).
- Villa I.M., Radiogenic isotopes in fluid inclusions, *Lithos* **55**, 2001, 115-124.
- Villa I.M., Hermann J., Müntener O. and Trommsdorff V., ^{39}Ar - ^{40}Ar dating of multiply zoned amphibole generations (Malenco, Italian Alps), *Contributions to Mineralogy and Petrology* **140**, 2000, 363-381.
- Villa I.M., Ruggieri G., Puxeddu M. and Bertini G., Geochronology and isotope transport systematics in a subsurface granite from the Larderello-Travale geothermal system (Italy), *Journal of Volcanology and Geothermal*

Research **152**, 2006, 20–50.

Vlasov N.G., Dyakov Y.A. and Cherev E.S., Geological Map of the Tajik SSR and Adjacent Territories, 1:500,000, 1991, VSEGEI (Vsesojuznoi Geol. Inst.); Leningrad, Saint Petersburg.

Wakabayashi J. and Dilek Y., Spatial and temporal relations between ophiolites and their subophiolitic soles: a test of models of forearc ophiolite genesis, In: Dilek Y., Moores E.M., Elthon D. and Nicolas A., (Eds.), *Ophiolites and Oceanic Crust: New Insights From Field Studies and the Ocean Drilling Program*, Geological Society of America, *Special Papers* **vol. 349**, 2000, 53–64.

Wakabayashi J. and Dilek Y., What constitute “emplacement” of an ophiolite?: **M**echanisms and relationship to subduction initiation and formation of metamorphic soles, In: Dilek Y. and Robinson **P.T.P.T.**, (Eds.), *Ophiolites i Earth History*, Geological Society of London, *Special Publications* **vol. 218**, 2003, 427–447.

Wetherill G.W., Discordant uranium–lead ages, *Transactions of the American Geophysical Union* **37**, 1956, 320–327.

Whattam S.A., Arc-continent collisional orogenesis in the SW Pacific and the nature, source and correlation of emplaced ophiolitic nappe components, *Lithos* **113**, 2009, 88–114.

Whattam S.A. and Stern R.J., The “subduction initiation rule”: a key for linking ophiolites, intra-oceanic forearcs, and subduction initiation, *Contribution to Mineralogy and Petrology* **Contributions to Mineralogy and Petrology** **162**, 2011, 1031–1045.

Yang T.N., Zhang H.R., Liu Y.X., Wang Z.L., Song Y.C., Yang Z.S., Tian S.H., Xie H.Q. and Hou K.J., Permo-Triassic arc magmatism in central Tibet: **E**vidence from zircon U-Pb geochronology, Hf isotopes, rare earth elements, and bulk geochemistry, *Chemical Geology* **284**, 2011, 270–282.

Yang Y., Guo Z. and Luo Y., Middle-Jurassic tectonostratigraphic evolution of Central Asia, implications for the collision of the Karakoram-Lhasa Block with Asia, *Earth-Science Reviews* **166**, 2017, 83–110.

Yin A. and Harrison T.M., Geologic evolution of the Himalayan-Tibetan Orogen, *Annual Review of Earth and Planetary Sciences* **28**, 2000, 211–280.

Zanchi A. and Gaetani M., Geological map of the north Karakorum terrain from the Chapursan Valley to the Shimshal Pass, Upper Hunza Valley, Pakistan, *Rivista Italiana di Paleontologia e Stratigrafia* **100** (1), 1994, 125–136.

Zanchi A. and Gaetani M., The geology of the Karakoram range, Pakistan: the new 1:100,000 geological map of Central-Western Karakoram, *Italian Journal of Geosciences* **130**, 2011, 161–262.

Zanchi A., Poli S., Fumagalli P. and Gaetani M., Mantle exhumation along the Tirich Mir Fault Zone, NW Pakistan: pre mid-Cretaceous accretion of the Karakoram terrane to the Asian margin, In: Khan M.A., Treloar P.J., Searle M.P. and Jan M.Q., (Eds.), *Tectonics of the Nanga Parbat Syntaxis and the Western Himalayas*, Geological Society of London *Special Publication* **vol. 170**, 2000, 237–252.

Zhang Y.C., Cheng L.R. and Shen S.Z., Late Guadalupian (Middle Permian) Fusuline fauna from the Xiala Formation in Xainza County, central Tibet: implication of the rifting time of the Lhasa Block, *Journal of Paleontology* **84**, 2010, 955–973.

Zhang Y.C., Shi G.R. and Shen S.Z., A review of Permian stratigraphy, palaeobiogeography and palaeogeography of the Qinghai-Tibet Plateau, *Gondwana Research* **24**, 2013, 55–76.

Zhang Y., Shen S., Zhai Q., Zhang Y. and Yuan D., Discovery of a Sphaeroschwagerina fusuline fauna from the Raggyorcaka Lake area, northern Tibet: implications for the origin of the Qiangtang Metamorphic Belt, *Geological Magazine* 2015, 1–7, <https://doi.org/10.1017/S0016756815000795>.

Zhao Z., Bons P.D., Wang G., Soesoo A. and Liu Y., Tectonic evolution and high-pressure rock exhumation in the Qiangtang terrane, central Tibet, *Solid Earth* **6**, 2015, 1–17.

Graphical abstract